OPTIMIZED RF SAFETY MONITORING FOR CEREBELLAR MAGNETIC RESONANCE IMAGING AT 7T

A THESIS SUBMITTED TO

THE GRADUATE SCHOOL OF ENGINEERING AND SCIENCE

OF BILKENT UNIVERSITY

IN PARTIAL FULFILLMENT OF THE REQUIREMENTS FOR

THE DEGREE OF

MASTER OF SCIENCE

IN

ELECTRICAL AND ELECTRONICS ENGINEERING

By

Elnaz Mahmoudi Mahmoudalilou

September 2024

Optimized RF Safety Monitoring for Cerebellar Magnetic Resonance Imaging at 7T
By Elnaz Mahmoudi Mahmoudalilou
September 2024

We certify that we have read this thesis and that in our opinion it is fully adequate, in scope and in quality, as a thesis for the degree of Master of Science.

Ergin Atalar(Advisor)

Emine Ülkü Sarıtaş Çukur

Yigitcan Eryaman

Approved for the Graduate School of Engineering and Science:

Orhan Arıkan
Director of the Graduate School

ABSTRACT

OPTIMIZED RF SAFETY MONITORING FOR CEREBELLAR MAGNETIC RESONANCE IMAGING AT 7T

Elnaz Mahmoudi Mahmoudalilou
M.S. in Electrical and Electronics Engineering
Advisor: Ergin Atalar
September 2024

The primary objective of this thesis is to develop optimized RF safety assessment techniques for cerebellar imaging using 7T MRI systems, with a specific focus on Spinocerebellar Ataxias (SCAs). Due to the unavailability of detailed electromagnetic simulation data from the manufacturer, this study focused on predicting the electromagnetic behavior of the Nova 8Tx/32Rx coil'S 8 pTx channels to ensure accurate and safe imaging. Accurate prediction of the coil's electromagnetic performance is essential for both RF safety and imaging quality, particularly in managing RF exposure and minimizing tissue heating.

The approach involved replicating the electromagnetic fields of the Nova coil through simulations, validating these predictions against experimental measurements, and implementing an algorithm for calculating the temperature-based Virtual Observation Points (tVOPs) in future works for rapid RF safety assessments. While the initial simulations captured key aspects of the coil's B_{1+} field distribution, discrepancies between predicted and experimental results revealed challenges, especially in random-phase shimming configurations. The limitations of using ideal current sources and the reduced dataset for optimization highlighted the need for more comprehensive data and realistic models.

The findings underscore the importance of integrating empirical measurements with refined simulations to bridge the gap between theoretical models and real-world performance. Future work should focus on enhancing current source models, mitigating noise and experimental inaccuracies, and expanding the application of these techniques to broader clinical scenarios. By addressing these challenges, this research can contribute to improving both the safety and quality of high-field MRI, ultimately advancing its reliability for both clinical and research

applications.

Keywords: 7T MRI, Parallel Transmission Prediction, Electromagnetic Simulations, RF Safety.

ÖZET

7T'DE SEREBELLUM MANYETIK REZONANS GÖRÜNTÜLEMESI IÇIN OPTIMIZE EDILMIŞ RF GÜVENLIK İZLEME

Elnaz Mahmoudi Mahmoudalilou
Elektrik ve Elektronik Mühendisliği, Yüksek Lisans
Tez Danışmanı: Ergin Atalar
Eylül 2024

Bu tezin temel amacı, 7T MRI sistemleri kullanarak serebellum görüntülemesinde RF güvenlik değerlendirme tekniklerini optimize etmektir; özellikle Spinocerebellar Ataksiler (SCAs) üzerinde durulmuştur. Üretici tarafından sağlanmayan ayrıntılı elektromanyetik simülasyon verilerinin eksikliği nedeniyle, bu çalışma Nova 8Tx/32Rx bobininin elektromanyetik davranışını tahmin etmeye odaklanmıştır. Bobinin elektromanyetik performansının doğru tahmini, hem RF güvenliği hem de görüntüleme kalitesi açısından, özellikle RF maruziyetini yönetmek ve doku ısınmasını en aza indirmek için hayati önem taşır.

Bu yaklaşım, Nova bobininin elektromanyetik alanlarını simülasyonlar yoluyla yeniden oluşturarak, bu tahminleri deneysel ölçümlerle doğrulamayı ve hızlı RF güvenlik değerlendirmeleri için sıcaklığa dayalı Sanal Gözlem Noktaları (tVOP'ler) uygulamayı içerir. İlk simülasyonlar bobinin B1+ alan dağılımının temel yönlerini yakalasa da, tahmin edilen ve deneysel sonuçlar arasındaki tutarsızlıklar, özellikle rastgele faz kaydırmalı yapılandırmalarda zorluklar ortaya çıkarmıştır. İdeal akım kaynaklarının kullanımı ve optimizasyon için azaltılmış veri seti, daha kapsamlı veri ve gerçekçi modellerin gerekliliğini vurgulamıştır.

Bulgular, teorik modeller ve gerçek dünya performansı arasındaki boşluğu kapatmak için ampirik ölçümler ile rafine edilmiş simülasyonların entegrasyonunun önemini vurgulamaktadır. Gelecekteki çalışmalar, akım kaynakları modellerini geliştirmeye, gürültü ve deneysel hataları azaltmaya ve bu tekniklerin daha geniş klinik senaryolara uygulanmasını genişletmeye odaklanmalıdır. Bu zorluklar ele alındığında, bu araştırma hem yüksek alan MRI'nin güvenliğini hem de kalitesini artırmaya katkıda bulunabilir ve nihayetinde klinik ve araştırma uygulamaları için güvenilirliğini ileriye taşıyabilir.

Anahtar sözcükler: 7T MRI, Paralel Transmisyon Tahmini, Elektromanyetik Simülasyonlar, RF Güvenliği .

Acknowledgement

I would like to express my deepest gratitude to my advisor, Prof. Ergin Atalar, for his invaluable guidance, support, and encouragement throughout the course of this research. His expertise and insights have been instrumental in shaping the direction of this work.

I am also grateful to the members of my thesis committee, Assoc. Prof. Emine Ülkü Sarıtaş Çukur and, Assoc. Prof. Yigitcan Eryaman for their constructive feedback and suggestions that significantly enhanced the quality of this thesis.

Special thanks to the SCAIFIELD consortium and all its members for their collaboration and support. Their collective efforts and dedication have provided a solid foundation for this research. I particularly acknowledge Prof. Dr. Tony Stöcker and his group members especially Sascha Brunheim for their assistance with the 7T MRI technology and transmit-array technology and providing the necessary resources and facilities to conduct this research.

I extend my gratitude to Prof. Pål Erik Goa for conducting the experiments for us. His meticulous work and dedication were essential in obtaining the critical data for this study.

I would like to extend my heartfelt thanks to the members of our group at UMRAM their continuous support and cooperation. Their contributions and encouragement have been invaluable.

I am profoundly grateful to Dr. Manouchehr Takrimi for his assistance and support during this research.

Lastly, I would like to thank my family and friends for their unwavering support and encouragement. Their patience and understanding have been a constant source of strength.

Contents

List of Figures

List of Tables

Chapter 1

Introduction

This thesis is about developing methods to predict the electromagnetic fields that NOVA 8TX RF coil generates inside the patient or phantom when used in parallel transmission (pTx) for 7T MRI systems. Understanding and controlling these electromagnetic fields is very important to ensure patient safety and get better image quality in a shorter time, especially in detailed imaging of the cerebellum for conditions like Spinocerebellar Ataxias (SCAs). The primary aim of this project was to create temperature-based Virtual Observation Points (tVOPs) to manage RF safety and improve 7T MRI.

Since we did not have access to detailed simulation design and data from the coil manufacturer, this study continued with predicting the electromagnetic properties of the Nova 8Tx/32Rx coil on our own. By simulating electric (E) fields and magnetic (B1+) fields, the future works of the project will focus on estimating the RF heating and temperature virtual observation points(tVOPs) and finding ways to optimize RF pulse sequences.

1.1 The SCAIFIELD Project

The SCAIFIELD consortium is a collaborative effort focused on improving the imaging techniques used to study Spinocerebellar Ataxias (SCAs), which are genetically heterogeneous, autosomal dominantly inherited neurodegenerative disorders. The consortium utilizes ultra-high field MRI (UHF-MRI) at 7T to provide unprecedented detail and sensitivity in imaging the cerebellum and brainstem, which are critically affected in SCAs. The project addresses significant technical challenges associated with 7T MRI, such as field inhomogeneities and RF safety, through the use of novel parallel transmission (pTx) MRI technology. By innovative RF pulse design, and rigorous validation methods, the consortium aims to establish new standards in MRI safety and effectiveness, facilitating the development of sensitive biomarkers for SCAs.

SCAIFIELD is organized into five primary work packages (WPs), each focusing on different aspects of MRI technology and imaging quality. Work Package 1 (WP1) is dedicated to developing and optimizing pTx technology to address RF inhomogeneity issues, especially in the cerebellum and brainstem. WP2 focuses on creating ultra-fast quantitative MRI (qMRI) sequences and refining molecular imaging techniques such as Chemical Exchange Saturation Transfer (CEST) and MR Spectroscopic Imaging (MRSI) for cerebellar applications. Work Package 3 (WP3) aims to develop robust quantitative MR parameter mapping and automated analysis pipelines to assess subtle pre-clinical and clinical alterations in SCAs. Work Package 4 (WP4) involves validating these advanced imaging techniques in a multicenter study of SCA mutation carriers and healthy controls, and translating the findings to more widely available 3T MRI systems. Finally, Work Package 5 (WP5), our group workpackage, focuses on improving RF safety and imaging quality by implementing temperature-based Virtual Observation Points (tVOP) calculations [3] for cerebellar imaging at 7T, reducing computation times and optimizing RF pulse sequences to enhance imaging quality and ensure patient safety. By addressing these diverse but interconnected areas, the SCAIFIELD project seeks to significantly enhance the diagnostic capabilities and safety of MRI for studying SCAs.

1.2 Motivation

Our project's primary aim was to develop and implement a temperature-based RF safety assessment technique for cerebellar imaging using 7T MRI systems, focusing on Spinocerebellar Ataxias (SCAs), for a European Union Joint Programme – Neurodegenerative Disease Research (JPND) project entitled 'Spinocerebellar Ataxias: Advanced Imaging with Ultra-High Field MRI' (SCAIFIELD) . The coordinator of this three-year (2021-2024) project is Prof. Dr. Tony Stoecker of German Center for Neurodegenerative Diseases.

This consortium uses 7T Siemens Terra scanners with transmit-array technology to obtain high-quality MR images. It is known that Siemens' RF safety limits are very conservative when applying RF pulses using their transmit array system. While this is good for patient safety, it may prohibit the usage of some pulse sequences. This conservative safety limit may increase the total scan time. Therefore, it is necessary to accurately calculate the head's temperature rise due to RF pulses exposure. Although electromagnetic and thermal models enable accurate calculation of the temperature rise, they are not feasible in scanning patients since the calculation time is prohibitively long. The built-in software of the scanner calculates local specific absorption rate (SAR) at some virtual observation points (VOP)[4]. As discussed in the original SCAIFIELD proposal, although the local SAR and local temperature rise are not related to each other, it has been shown that in the regions of high perfusion, the temperature will not elevate significantly even with high local SAR. On the other hand, one may observe a high-temperature rise in the areas with low perfusion[3]. Therefore, manufacturers have to use a wide safety margin to ensure safety.

We planned to implement temperature based virtual observation point (tVOP) [3] calculation for the cerebellar imaging at 7T. This would significantly decrease the necessary computation time and enable fast and accurate estimates. In the calculation, the electromagnetic simulations of the RF coil would be used.

Electromagnetic simulations play a crucial role in these safety calculations.

They allow us to predict the distribution of electrical fields (E-fields) and magnetic fields (B1-fields) within the human body or a phantom model. The E-fields are particularly important because they directly relate to the Specific Absorption Rate (SAR), which quantifies the rate at which energy is absorbed by the body and consequently converted into heat [5].

Initially, our project relied on the electromagnetic simulation design of the head coil from Siemens. However, due to the unavailability of this simulation data, we had to proceed with Plan B, which involved predicting the 8Tx configuration of the transmit coil used in the project (8Tx32Rx 7T Head Coil Clinic Model 8893279). In this text, this coil will be refered as the Nova Coil. The first step in this alternative plan involved predicting the electromagnetic simulation of the Nova coil to calculate the E fields inside the phantom.

Once we have accurate E-field distributions, we can develop an algorithm to calculate temperature matrices from the Q matrices. These temperature matrices will allow us to determine the local temperature rise at different points within the phantom, leading to the calculation of temperature-based Virtual Observation Points (tVOPs). These tVOPs can then be used to optimize the RF pulse sequences, enhancing imaging quality while ensuring patient safety [3].

Recent advancements propose calculating local temperature rise rather than SAR to provide a more accurate safety measure, reducing the need for conservative safety margins. The tVOP method, proposed by Boulant et al. [3], offers a promising solution by calculating temperature rise at selected points, potentially optimizing RF pulse sequences without compromising safety. There are different methods to calculate the tVOPs. One suggested method, proposed by Eichfelder et al. [4], clusters the Q matrices of the phantom. Another method searches for the tVOPs without clustering [6]. Additionally, an improved compression method is proposed by Orzada et al. [7]. Incorporating the National Magnetic Resonance Research Center (UMRAM) into the SCAIFIELD consortium aims to leverage this technique, hypothesizing that tVOP can predict maximum temperature rise and optimize pTx RF pulses to minimize body temperature increases, thus improving imaging quality.

Our future studies will focus on demonstrating the practical application of the tVOP method in overcoming technical challenges in 7T MRI. By standardizing MRI-related RF heating problems and improving safety protocols, we aim to support the clinical trials involving SCAs and contribute to the development of safer and more effective imaging techniques [4, 8].

1.3 The Objective and Scope of the Thesis

This thesis focuses on the development and implementation of technique for predicting the electromagnetic behavior of RF coils, specifically for use with parallel transmission in 7T MRI systems. Accurate prediction and control of the electromagnetic fields are crucial for ensuring patient safety and improving the quality of imaging, particularly in advanced applications such as those targeting neurodegenerative disorders.

Initially, for safety assessments, we relied on the electromagnetic simulation design from Siemens, which was unavailable. Consequently, we proceeded with Plan B, predicting the Nova coil's 8Tx configuration ourselves. This step involved predicting the coil's electromagnetic simulation fields to calculate the Q matrices inside the phantom, which is crucial for safety assessments. These Q matrices represent the relationship between the applied RF pulses and the resulting E-field distributions.

Following this, we developed an algorithm to calculate temperature matrices from the Q matrices. These temperature matrices allow us to determine the local temperature rise at different points within the phantom. While the ultimate goal includes using these matrices for calculating temperature-based Virtual Observation Points (tVOPs), our primary focus was on the accurate prediction and validation of the coil's electromagnetic behavior.

To achieve this aim, first, we designed a coil and optimized it using a spherical reference phantom's Electromagnetic fields. Then, the validation of the predicted electromagnetic behavior was conducted through measurements performed at Bonn's 7T pTx system and Trondheim's facilities, ensuring the accuracy and reliability of the Q matrix predictions and the overall safety of the imaging protocols.

The scope of this thesis includes:

- The development of predictive methods to simulate the Nova coil and understand its behavior in generating electrical fields inside a phantom.
- Conducting experimental validation through phantom measurements to validate the coil simulation, ensuring the accuracy and reliability of the predicted electromagnetic behavior.

Ultimately, these methods will provide a foundation for future work on integrating temperature-based RF safety assessments into existing imaging protocols of the SCAIFIELD consortium and applying them to real-world scenarios involving advanced MRI applications.

This thesis is structured into six chapters. Chapter 1 introduces the study, explaining the motivation behind the research, providing a comprehensive literature survey, and outlining the objectives and scope of the thesis. Chapter 2 delves into the background and foundations for the research, covering essential topics such as MRI signal formation, RF fields, parallel transmission, RF heating, and RF safety constraints. Chapter 3 describes the method used for predicting the electromagnetic behavior of the Nova coil. Chapter 4 details the experimental setups and procedures followed, including the algorithms implemented for the prediction of the electromagnetic behavior and the calculation of temperature matrices. Chapter 5 presents the results of the experiments and simulations, including validation of the predicted electromagnetic behavior through phantom measurements. Chapter 6 discusses the findings and their implications for RF safety and imaging quality, focusing on the practical application and accuracy of the coil prediction method and its potential to enhance 7T MRI imaging and finally, concludes the thesis with a summary of the work conducted and suggestions for future research, highlighting the contributions of the thesis to the field of high-field MRI and discussing the next steps for integrating temperature-based RF safety assessments into existing imaging protocols. The outcomes will directly support the goals of the SCAIFIELD consortium and facilitate the development of more precise and reliable imaging biomarkers for use in clinical trials.

Chapter 2

Theoretical Background

2.1 Introduction

This chapter provides the theoretical background necessary to understand the theory, methodologies, and analyses presented in this thesis. It covers the fundamental principles of MRI signal formation and RF fields, the technology of parallel transmission and its implications for RF heating, and the safety constraints associated with RF fields in MRI. Understanding these concepts is crucial for the development and implementation of 8Tx Nova head coil (8Tx32Rx 7T Head Coil Clinic Model 8893279, Nova Medical, Inc., Wilmington, MA, USA) prediction and temperature-based RF safety assessment techniques for cerebellar imaging using 7T MRI systems.

2.2 MRI Signal Formation

MRI signal formation is based on the principles of nuclear magnetic resonance (NMR). The fundamental unit of MR signal comes from hydrogen nuclei (protons) in the body, which are abundant due to the high water and fat content in tissues.

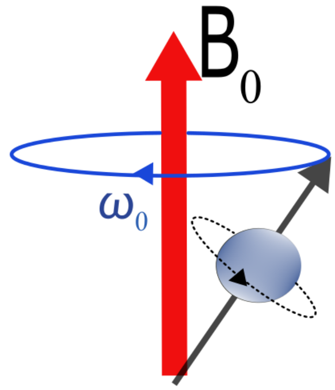

Figure 2.1: The precession of an atomic nucleus around an external magnetic field B_0 is depicted, with the nucleus rotating at the Larmor frequency ω_0 around B_0 (indicated by the blue arrow), while it also rotates around its own axis.

When placed in a strong static magnetic field (B_0), the magnetic moments of hydrogen nuclei align with the magnetic field. These aligned nuclei precess around the direction of the magnetic field at a specific frequency called the Larmor frequency (ω_0), which is given by:

$$\omega_0 = \gamma B_0 \tag{2.1}$$

where γ is the gyromagnetic ratio, a constant specific to hydrogen or any given nuclei [9]. The precession of an atomic nucleus around an external magnetic field B_0 is depicted in Figure 2.1.

To detect signals from atomic nuclei in equilibrium with respect to B_0, the net equilibrium magnetization M_0 must be perturbed so that a component lies orthogonal to the B_0 field. This excitation is achieved using a radiofrequency (RF) electromagnetic field B_1, which rotates the magnetization by an angle θ, known as the flip angle. For a general RF pulse, the flip angle is calculated by integrating the RF magnetic field $B_1(t)$ over the duration of the pulse:

$$\theta = \gamma \int_0^\tau B_1(t)\, dt \tag{2.2}$$

where:

- γ is the gyromagnetic ratio. $B_1(t)$ is the time-dependent RF magnetic field amplitude. τ is the duration of the RF pulse.

The B_1 field is much smaller in magnitude than the B_0 field and is set to the Larmor frequency ω_0 [9].

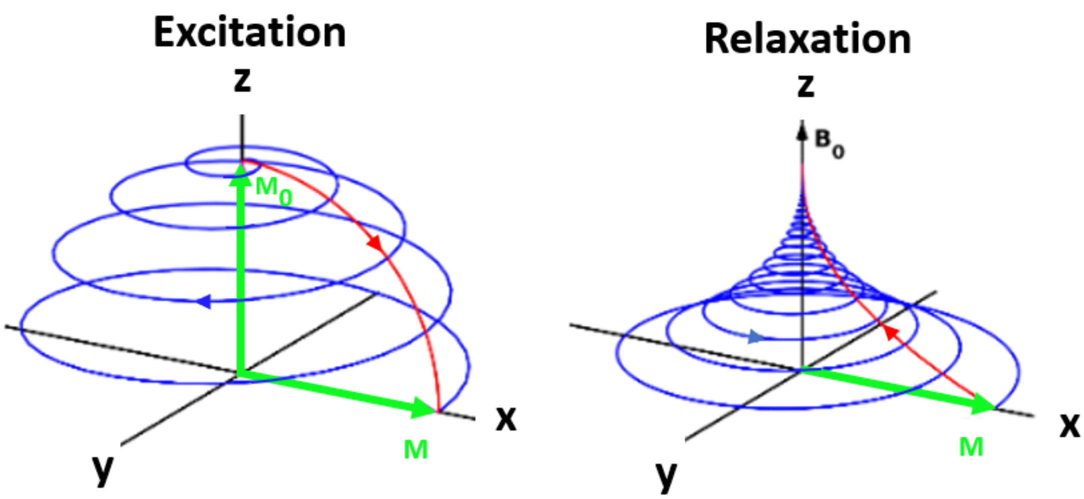

Figure 2.2: Illustration of the excitation of a magnetization vector (left) and its relaxation back to equilibrium (right). The red line indicates the movement in the rotating frame of reference, while the blue line depicts the movement in the laboratory frame, with the vector oscillating at the Larmor frequency ω_0.

After the RF pulse is turned off, the hydrogen nuclei return to their equilibrium state (realign with B_0). This process is called relaxation and occurs in two phases: T1 (longitudinal) relaxation and T2 (transverse) relaxation. During relaxation, the nuclei emit RF signals that are detected by RF Rx and used to reconstruct images based on their frequency and phase information [10].

2.3 RF Fields

An RF pulse is a short burst of radio waves used to perturb the magnetic moments of hydrogen nuclei. The RF pulse is characterized by its frequency, duration, and amplitude, and it must match the Larmor frequency of the hydrogen nuclei to be effective.

The RF field in MRI, referred to as the B_1 field, is responsible for exciting the hydrogen nuclei. This field is generated by RF coils, which are also used to receive the emitted signals. The B_1 field must be homogeneous to produce high-quality images. The B_1 field can be divided into two components: B_{1+}, the transmit field, and B_{1-}, the receive field. For optimal imaging, B_{1+} should be uniform across the region of interest (ROI)[1].

The B_1 field is specifically designed to interact with the nuclear magnetic resonance process, operating within the plane perpendicular to the B_0 field, namely the x-y plane. When the overall B_1 vector is generated, its behavior can be analyzed within a rotating frame at an angular frequency ω[1].

If the laboratory and rotating frames coincide at $t = 0$, then at a later time t, the rotating frame's axes (denoted with tildes) form an angle ωt with the laboratory frame. This is illustrated in Figure 2.3, where the laboratory frame is depicted with black lines and the rotating frame with blue lines. The positively rotating frame forms an angle $+\omega t$ with the laboratory frame (left side of the figure), while the negatively rotating frame forms an angle $-\omega t$ (right side of the figure)[1].

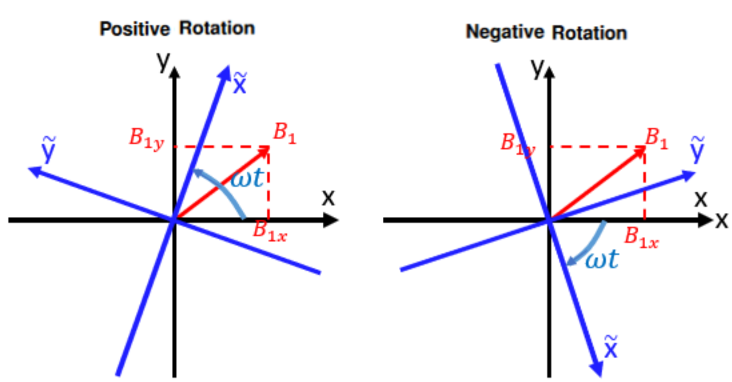

Figure 2.3: Coordinate systems for the positively (left) and negatively (right) rotating frames are illustrated. The black axes represent the laboratory reference frame, while the blue axes denote the rotating frames. The B_1 vector is depicted in red[1].

for an Argand diagram representation where complex numbers are on the $\tilde{y}$ axis and real numbers on the $\tilde{x}$ axis, the B_1 fields in the positive and negative rotating frames produced by an RF coil can be shown as[1]:

$$\tilde{B}_1^+ = \frac{B_{1x} + iB_{1y}}{2}$$
$$\tilde{B}_1^- = \frac{(B_{1x} - iB_{1y})^*}{2}$$

These are extremely important expressions in MRI as, depending on the relative orientation of the B_0 field, one of these will represent the transmit B_1 field, and one will represent the receive field[1]. Generally, $\tilde{B}_1^+$ is the transmit field and $\tilde{B}_1^-$ is the receive field. From this expression, the efficiency of transmission and reception under different polarizations can be considered[1].

It is important to clarify that within this thesis, analyses of RF fields, especially those concerning the transmit B_1 fields, will utilize phasor notation. This approach represents the fields as complex numbers at a single frequency, simplifying the calculations and understanding of their interactions within the MRI system. The components B_{1x} and B_{1y}, representing the x and y components of the RF magnetic field, will be considered within the rotating frame of reference and analyzed using this notation.

2.4 Ultra-High Field MRI

In the context of technological advancements in MR hardware, especially in the areas of magnets, gradients, and transmit/receive coils, the development of fast and ultra-fast imaging has become possible [11, 12]. Additionally, there is a trend towards increasing static field strengths [11, 13]. The increase in static magnetic field strength in the human field ranges from initially 0.1T to currently up to 11.7T [13]. In the clinical field, devices with 1.5T, 3T and 7T are in use, while higher magnetic field strengths are currently only used in clinical research [13].

The great interest in higher field strengths has various reasons. With increasing field strength, the polarization of the magnetic moments by the external field increases [11, 12]. The energy difference between parallel and antiparallel oriented moments is directly proportional to the field strength B_0 according to Eq. 2.3 [14]. At a field strength of 7T, the energy difference is almost ten times higher compared to a field strength of 1T. For this reason, the parallel alignment becomes more attractive with increasing field, and the excess of parallel-oriented moments becomes larger. For 7T, the excess of parallel-oriented magnetic moments is 50ppm. Accordingly, more excess magnetic moments are available for polarization [11].

As can be seen from Curie's law (Eq. 2.3), the magnetization M_0 is directly proportional to the field strength B_0 at constant temperature [11]:

$$M_0 \propto B_0 \tag{2.3}$$

Since the measurement signal is directly proportional to the transverse magnetization M_{xy} according to Equation 2.9, which in turn is proportional to the initial magnetization M_0 (Equation 2.10), the strength of the measurement signal is also directly proportional to the field strength. Furthermore, the signal induced in the receive coil is directly proportional to the Larmor frequency. Therefore, the increased signal intensity with increasing field strength is not only due to stronger polarization but also due to higher induced voltage in the receive coil due to the higher Larmor frequency[14].

As the signal increases, the SNR increases [11]. Since the SNR is proportional to the voxel volume, a gain in SNR through higher static field strengths can be invested in a reduced voxel volume and thus higher spatial resolution [15, 16]. Alternatively, the higher SNR can also be converted into higher temporal resolution and used to shorten the acquisition time T_{acq} while maintaining image quality, as the SNR $\propto \sqrt{T_{acq}}$ [15].

2.5 Parallel Transmission

In the 1980s, coils were introduced that have not just one, but multiple independent receiving channels [17]. The "parallel imaging" enabled by these coils offers many advantages over the previously used single-channel coils. These advantages include improved signal-to-noise ratio (SNR) and the possibility of faster imaging through reduced measurement times [17, 18].

Building on this development, the concept of coil arrays was extended to the transmission of RF pulses. In multi-channel transmission, instead of just one coil, multiple parallel coil elements are used to transmit the RF excitation pulses [17]. This allows each coil element to be driven independently and assigned individual amplitude and phase, or even completely different pulse shapes [19].

The resulting total field $B_{1,\mathrm{tot}}$ is obtained by superimposing the complex-valued individual fields $B_{1,i}$, which are composed of the coil sensitivity $S_{B1,i}$ and the channel weighting w_i [20]:

$$B_{1,\mathrm{tot}} = \sum_i B_{1,i} = \sum_i S_{B1,i} w_i \tag{2.4}$$

The channel weighting is complex-valued and has an amplitude and a phase component [20]:

$$w_i = A_i \cdot e^{j\phi_i} \tag{2.5}$$

The amplitude of a channel corresponds to the current or voltage amplitude needed to generate an RF pulse of a certain strength. The coil sensitivity refers to the field distribution produced per unit of current or voltage. By varying amplitude and phase, the resulting B_1 field can be influenced [20].

This method improves the homogeneity of the B_1 field generated by the RF pulses, ensuring uniform intensity and contrast in the examined area. This is particularly advantageous for ultra-high field (UHF) imaging [21].

The process of varying these coil parameters to improve imaging is known as B_1 or RF shimming [22, 17].

2.5.1 Basics of Parallel Transmission

In conventional single-channel transmission systems, the B_{1+} field can be inhomogeneous, especially at higher field strengths. This inhomogeneity leads to variations in signal intensity across the image, resulting in artifacts and reduced image quality. pTx systems overcome this by adjusting the phase and amplitude of the RF pulses for each channel, creating a more uniform B_{1+} field. In a pTx system, each RF coil element is driven by an independent amplifier. This setup allows individual control over the amplitude and phase of the RF pulses delivered by each coil element. The independent control over each coil element's RF pulses enables precise manipulation of the B_{1+} field, optimizing it for uniformity and efficiency across the entire region of interest. The principle behind pTx is the ability to manipulate the spatial distribution of the RF field [23].

2.5.2 Designing the Coil Array

Designing the coil array for pTx involves selecting the appropriate number of coil elements and their configuration. The coil elements must be arranged to cover the region of interest uniformly and provide the necessary field strength. Common configurations include arrays of loop or stripline coils, which can be tailored to the specific anatomical region being imaged [24]. The design process also involves tuning each coil element to the Larmor frequency of the magnetic field strength used in the MRI system. This ensures that the RF pulses are efficiently transmitted and received. The coils must also be decoupled from each other to prevent interference and signal loss. Decoupling techniques include geometric decoupling and employing overlapping coil elements [25].

2.5.2.1 Microstripline Coils

Microstripline coils, also known as microstrip RF coils, are another type of RF coil used in high-field MRI and spectroscopy. These coils are particularly advantageous for ultra-high-field applications due to their ability to generate highly localized B_1 fields with efficient transmission characteristics. The microstripline design involves a strip of conductive material placed over a ground plane, separated by a dielectric layer. This configuration forms a transmission line that can be precisely tuned to the desired Larmor frequency [26].

The design of microstripline coils is similar to that of stripline coils[27] but with some notable differences. In microstripline coils, the conductive strip is typically narrower, and the ground plane is closer to the strip, which enhances the confinement of the electromagnetic fields and improves the coil's efficiency. This design allows for better control over the B_1 field distribution, making microstripline coils well-suited for applications requiring high spatial resolution and sensitivity [26].

Microstripline coils offer several advantages for MRI and spectroscopy. They provide high Q-factors, which indicate efficient energy transmission and reception, and their design allows for easy integration into multi-channel coil arrays. Additionally, microstripline coils can be designed to be flexible, which is beneficial for imaging various anatomical regions. The high efficiency and localized field generation make microstripline coils an excellent choice for ultra-high-field MRI, where precise control of the B_1 field is essential [26].

2.5.3 Benefits of Parallel Transmission

pTx systems significantly reduce the inhomogeneity of the B_{1+} field, a common issue in high-field MRI [28]. This improvement is crucial for obtaining high-quality images and ensuring that the RF energy is evenly distributed across the scanned area. The enhanced homogeneity translates to fewer artifacts and more consistent signal intensity across the image, improving diagnostic accuracy [25]. With more uniform B_{1+} fields, the resulting images have fewer artifacts and better signal consistency. This uniformity helps in obtaining clearer and more diagnostic images. Enhanced image quality is particularly important in clinical applications, where accurate imaging is critical for diagnosis and treatment planning [28].

Parallel transmission allows for greater flexibility in designing imaging protocols. By adjusting the RF pulses' phase and amplitude, different imaging sequences can be tailored to specific clinical needs. This flexibility enables the development of specialized protocols for various anatomical regions and clinical indications [29]. With optimized B_{1+} field distribution, pTx systems can potentially reduce scan times. Faster scans are beneficial in clinical settings, as they increase patient throughput and reduce discomfort for patients. Additionally, shorter scan times can minimize motion artifacts, further improving image quality [23].

2.5.4 Optimizing Pulse Sequences

Once the pTx system is calibrated, pulse sequences must be optimized to take full advantage of the system's capabilities. Pulse sequence optimization involves adjusting the RF pulses' timing, amplitude, and phase to maximize the uniformity of the B_{1+} field and minimize artifacts [29]. In pTx systems, advanced pulse design techniques, such as parallel transmission pulse design and RF shimming, are used. These techniques involve calculating the optimal RF pulses for each channel to achieve the desired B_{1+} field distribution. The optimization process considers factors such as the anatomical region being imaged, the desired contrast, and the specific imaging sequence used [25].

A commonly used optimization approach for RF shimming is the least-squares method, which minimizes the difference between the desired target magnetization and the actual magnetization produced by the coil array. This can be expressed as:

$$\arg\min_w \|S \cdot w - m_{\text{targ}}\| \tag{2.6}$$

where S is the system matrix containing the sensitivities of the coil elements, w is the vector of complex weightings for each channel, and m_{targ} is the target magnetization.

2.5.5 Challenges and Considerations

While pTx offers significant advantages, it also presents several challenges and considerations. Implementing pTx systems is more complex and costly than traditional single-channel systems. The need for multiple RF amplifiers, advanced coil arrays, and sophisticated calibration techniques adds to the overall expense and complexity of the system [24]. Regular calibration and maintenance are essential to ensure optimal performance of pTx systems. This requires specialized knowledge and equipment, increasing the operational demands on imaging facilities. Ensuring proper decoupling of coil elements and minimizing electromagnetic interference is critical for achieving accurate and reliable results. This requires careful design and testing of the coil array and associated electronics [25].

2.6 RF Heating

RF heating in MRI refers to the energy deposition from RF fields within a subject, quantified by specific absorbtion rate(SAR). SAR, expressed in watts per kilogram (W/kg), measures the rate of energy absorbed by tissues. Managing SAR is critical due to regulatory constraints set by bodies like the FDA and IEC to prevent excessive heating [25, 30].

The specific absorption rate (SAR) is a measure of the absorption of electromagnetic fields in biological tissue [20, 15]. Apart from the strong inhomogeneities of the magnetic field with increasing field strength, management of high SAR is one of the biggest challenges of UHF MRI imaging, as it increases quadratically with increasing amplitude of the B_1 field and increasing Larmor frequency [12]. High SAR causes temperature increase and excessive temperature increase causes tissue damage and hyperthermia.

Due to the electromagnetic alternating fields, electric currents are induced in the body according to Faraday's law. This energy input, or the associated losses, causes heating of the absorbing material [15]. This can irreversibly damage the tissue. For this reason, the temperature increase of the tissue must be kept below specific limits. Typically, temperature increases of more than 1°C should be avoided [25].

Since local temperature changes in the human body cannot be measured directly, the energy input from the RF pulses is quantified using SAR (Eq. 3.10). The maximum permissible SAR and the resulting temperature increases are regulated by various international standards of the International Electrotechnical Commission (IEC) and the American Food and Drug Administration (FDA) (see Table 2.1) [25, 30].

There are three different operating modes, which differ essentially in the required safety and monitoring measures with regard to gradient power and SAR values [25, 30].

In addition, limits are defined for different body regions. Whole body SAR refers to SAR values averaged over the entire body and total body weight. Accordingly, the global head SAR is averaged over the entire head mass [2]. For the local value, the SAR values are not averaged over larger body areas but over volume fractions with a total mass of 10g [2].

Furthermore, there is a short-term SAR limit where the values must not exceed two times the specified values for the respective operating mode and body region within a period of 10 seconds [25].

Since local SAR cannot be measured directly, SAR monitoring is usually based on electromagnetic simulations. The SAR can be estimated from the generated

Operating Mode	Whole Body (global, W/Kg)	Head (global, W/Kg)	Head (local, W/Kg)
Normal	2	3.2	2-10
Controlled 1st level	4	3.2	4-10
Controlled 2nd level	>4	>3.2	>(4-10)

Operating Mode	Maximum Core Temperature (°C)	Rise of Core Temperature (°C)
Normal	38	0.7
Controlled 1st level	38.5	1.3
Controlled 2nd level	>38.5	>1.3

Table 2.1: International SAR and temperature limits of the IEC. The global SAR values are averaged over a specific body region. The local SAR is obtained from the SAR values averaged over 10g volume fractions [2].

models [20]. In practice, the real-time calculation of the maximum SAR for a given RF pulse is important, ensuring that the limits are not exceeded during an ongoing MRI scan [20].

For this purpose, the power supplied to the transmit coil and the power reflected by it are continuously measured. The difference between the two values represents the accepted power. The accepted power, together with an SAR model obtained from simulations, allows the calculation of SAR during the scan [20].

Especially with multi-channel transmit coils, the distribution of SAR in the examined volume can vary greatly depending on the channel configuration, complicating real-time SAR monitoring compared to single-channel systems [20]. Moreover, due to the physical conditions, so-called hotspots are increasingly formed, areas where locally very high SAR values occur [20].

The information gained about the SAR characteristics of a coil or a coil array can be used for RF shimming or pulse design. The excitation pulses can be designed to achieve the desired field distribution while complying with the SAR limits [31, 6]. The process of SAR monitoring and regulation is referred to as SAR management [20].

2.7 Calculating the thermal virtual observation points (tVOPs)

Accurately predicting and managing radiofrequency (RF) exposure is critical for the safety of MRI procedures, especially with high-field systems like 7T MRIs. The human body's complex response to RF energy requires sophisticated models to assess safety risks and ensure regulatory compliance. This section describes how we calculate the Specific Absorption Rate (SAR), develop Q-matrices for simpler calculations in parallel transmission systems, and use thermal virtual observation points (tVOPs) to manage temperature increases. This section will be essential for future works, after predicting the coil design the next step is to calculate the tVOPs for pulse design.

2.7.1 SAR Calculation

Specific Absorption Rate (SAR) is induced by the electric fields generated by the RF coil. Since direct real-time measurement of SAR is challenging, simulations are typically used to estimate SAR based on the electric field distribution and tissue properties. The fundamental formula for SAR at a given point r is expressed in terms of the peak electric field as:

$$\mathrm{SAR}(r) = \frac{\sigma(r)}{2\rho(r)}|E(r)|^2 \tag{2.7}$$

where σ is the electrical conductivity, ρ is the mass density, and $E(r)$ is the peak amplitude of the electric field vector at location r. This formulation uses phasor notation, representing the steady-state peak values of the electric field. Temporal variations in the electric field are accounted for by assuming a sinusoidal oscillation at the Larmor frequency, but they are not explicitly included in the SAR calculation.

For regulatory compliance, SAR is typically averaged over a defined volume

V, such as 1g or 10g of tissue [3]:

$$\mathrm{SAR}_{\mathrm{avg}} = \frac{1}{V}\int_V \frac{\sigma(r)}{2\rho(r)}|E(r)|^2 dV. \tag{2.8}$$

This averaging process ensures that the calculated SAR values reflect the regulatory limits for safe RF exposure across different tissue types and volumes.

2.7.2 Q-matrices

In parallel transmission (pTx) systems, computing SAR for various channel inputs is simplified using Q-matrices, representing the inter-coil coupling and SAR sensitivities. If $E_c(r)$ is the electric field produced by the unit excitation of channel c, the electric field E with dimensionless weighting w is:

$$E(r,t) = \sum_{c=1}^{N_c} E_c(r) \cdot I_c(t) \tag{2.9}$$

The SAR is then computed as:

$$\mathrm{SAR}(r,t) = \frac{1}{V}\int_V \frac{\sigma(r)}{2\rho(r)}\left|\sum_{c=1}^{N_c} E_c(r)\cdot I_c(t)\right|^2 dV = I(t)^* \cdot Q(r) \cdot I(t) \tag{2.10}$$

where Q is the Q-matrix for location r :

$$Q(r) = \frac{\sigma}{2\rho}\left(\mathbf{E}_{cx}\mathbf{E}_{cx}^* + \mathbf{E}_{cy}\mathbf{E}_{\mathbf{cy}}{}^* + \mathbf{E}_{cz}\mathbf{E}_{cz}^*\right) \tag{2.11}$$

where $\mathbf{E}_{xyz}$ is the normalizedcomplex row vector containing the electric field valuescoming from each channel and for the corresponding axis, at location r [3].

The SAR can be calculated using Q(r) Hermitian local matrices defined for every voxel as Eq. 2.10. Given N_t-point time waveforms dispatched on N_c channels, I_c being the N_t by N_c array containing all these waveforms, for 100% duty cycle, the SAR at voxel r is given by:

$$\text{SAR}(r) = \sum_{i,j}^{N_c} Q_{i,j}(r) \cdot \frac{1}{N_t} \sum_{k}^{N_t} \left(I_c^*(t_k) I_c(t_k) \right)_{i,j} \tag{2.12}$$

2.7.3 Virtual Observation Points (VOPs)

For peak local SAR prediction of given human model, transmit array configuration and a fixed relative geometry between the model and the array, the number of complex multiplications are $N.N_c.N_c$ which N is the number of voxels inside the model. To handle the vast number of Q-matrices in voxel models which can be more than millions, Virtual Observation Points (VOPs) compress these matrices, reducing computational load. VOPs represent clusters of Q-matrices, ensuring the maximum local SAR estimation remains accurate without evaluating every matrix. The process involves clustering mathematically similar matrices and finding a minimal solution for overestimation, producing fewer VOPs with controlled overestimation factor ϵ[4].

2.7.4 Thermal Model

A general linear absolute temperature model may be written as:

$$\rho c_p \frac{\partial T}{\partial t} = f(T) + g + \rho \cdot \text{SAR}, \tag{2.13}$$

where ρ is the tissue density (kg/m^3), c_p the specific heat capacity (J/kg/K), T the local temperature (K), and f is a linear function of temperature. The term g is independent of the RF source and of the temperature. It leads to a nonzero equilibrium temperature in the absence of RF[3]:

$$f(T_{\text{eq}}) + g = 0, \tag{2.14}$$

which simply expresses the balance between heat production (e.g., with metabolism) and heat losses (conduction, perfusion) in this condition. All terms may be spatially dependent. In the case of Pennes' bio-heat model, the different terms are[3]:

$$f(T(\mathbf{r})) = \vec{\nabla} \cdot (k(\mathbf{r})\vec{\nabla}T(\mathbf{r})) - B(\mathbf{r})T(\mathbf{r}), \tag{2.15}$$

and

$$g(\mathbf{r}) = B(\mathbf{r})T_b(\mathbf{r}) + C(\mathbf{r}), \tag{2.16}$$

where k is the thermal conductivity (W/K/m), B the perfusion constant (W/K/m^3), T_b the time-independent (but possibly spatially dependent) blood temperature (K), and C is the metabolic rate (W/m^3)[3].

Exploiting the linearity of f and setting the absolute temperature $T(\mathbf{r})$ equal to the equilibrium temperature $T_{\text{eq}}(\mathbf{r})$ plus the temperature rise $\Delta T(\mathbf{r})$ yields for the latter[3]:

$$\rho c_p \frac{\partial \Delta T}{\partial t} = f(\Delta T) + \rho \cdot \text{SAR}, \tag{2.17}$$

i.e., g, which contains T_b and C in the case of Pennes' model, drops out of the equation. In this description, the temperature rise thus does not depend on the equilibrium temperature and on some possibly uncertain function g[3].

2.7.5 Temperature Matrices

Equation [3] being linear with respect to the RF heat source, one can numerically solve it for each $Q_{i,j}(r)$ map to obtain for a given duration a corresponding $\Delta T_{i,j}(r)$ complex distribution which is a solution of:

$$\rho c_p \frac{\partial \Delta T_{i,j}(r)}{\partial t} = f(\Delta T_{i,j}(r)) + \rho Q_{i,j}(r) \tag{2.18}$$

Because $Q_{i,j}(r)$ and $Q_{j,i}(r)$ are complex conjugates, by construction so are $\Delta T_{i,j}(r)$ and $\Delta T_{j,i}(r)$. Hence, after $N_c(N_c+1)/2$ computations, by exploiting the linearity of the model, the temperature rise $\Delta T(r)$ at any point can be calculated using $T(r)$ complex matrices:

$$T(r) = \begin{bmatrix} \Delta T_{1,1}(r) & \cdots & \Delta T_{1,N_c}(r) \\ \vdots & \ddots & \vdots \\ \Delta T_{N_c,1}(r) & \cdots & \Delta T_{N_c,N_c}(r) \end{bmatrix} \tag{2.19}$$

For any waveform array $\mathbf{I}_c$, one obtains:

$$\Delta T(r) = \sum_{i,j}^{N_c} \Delta T_{i,j}(r) \cdot \frac{1}{N_t} \sum_{k}^{N_t} \left(I_c^*(t_k) I_c(t_k)\right)_{i,j} \tag{2.20}$$

For a static RF shim with $\mathbf{x}$ the vector containing the N_c complex weights, the previous result becomes:

$$\Delta T(r) = \mathbf{x}^* T(r) \mathbf{x} \tag{2.21}$$

2.7.5.1 Compression Scheme

Drawing the parallel with the SAR and the Q matrices, a similar Temperature VOP (TVOP) compression scheme can be derived. By defining ΔT_G as the average temperature rise over the whole volume, one can define the TVOPs as the set of T matrices, which guarantees that there exists a $k \in$ TVOPs such that:

$$\Delta T_k \leq \max(\Delta T(r)) \leq \Delta T_k + \lambda \Delta T_G \tag{2.22}$$

where λ is the tolerance factor that controls the level of compression and ΔT_k denotes the temperature rise calculated for the k-th TVOP. Following the work in Lee et al.[6] and Orzada et al.[7], the T matrices are first sorted according to their maximum eigenvalues in decreasing order. The set of TVOPs is then initialized as the first T matrix in the list. The algorithm proceeds to search for a set of N positive coefficients c_n, with N being the current number of TVOPs, whose sum is unity $\sum_{n=1}^{N} c_n = 1$, and such that:

$$\sum_{n=1}^{N} c_n \mathrm{TVOP}_n + \lambda T_G - T \geq 0 \tag{2.23}$$

where T is a candidate TVOP and T_G is the global temperature matrix. If such a set of coefficients is found, the candidate T matrix is not retained as a TVOP.

2.7.6 Voxel Models

Voxel models derived from MRI or CT scans, segmented into different tissues, are used for SAR simulations. These models represent different body types and are essential for accurate SAR assessment. Individualized models, created from quick scans, aim to match specific subjects, though full EM simulations remain time-consuming [4].

By understanding and leveraging these concepts, RF heating in MRI can be effectively managed, ensuring patient safety and adherence to regulatory standards.

Chapter 3

Theory

3.1 Introduction

As discussed in Chapter 1, for safety assessments, it is crucial to determine the electrical fields induced by the Nova coil inside a phantom. This requires electromagnetic simulation of the Nova coil, which is not provided by the manufacturer. Therefore, the goal is to predict a coil that replicates the electromagnetic behavior of the Nova coil. This chapter delves into the theoretical foundation and practical methodologies for predicting and verifying the performance of MRI RF coils. It focuses on replicating the B_1 and E fields of the Nova 8Tx/32Rx head coil by designing microstripline configurations and optimizing current sources to achieve field distributions comparable to those of the reference coil. This approach ensures consistent MRI application outcomes, facilitating reliable and safe imaging procedures.

Furthermore, this chapter explores the verification process of electric fields through induced temperature rise in tissue-equivalent phantoms. Employing specific absorption rate (SAR) measurements and electromagnetic simulations, the study validates the safety and efficacy of the RF coil designs. The combination of theoretical insights and practical techniques outlined in this chapter provides a comprehensive framework for developing and validating MRI RF coils, emphasizing the importance of precise electromagnetic simulations and accurate field replication to ensure patient safety and optimal imaging performance.

3.2 Predicting the Nova head coil

In this study, the aim was to predict a coil that accurately replicates the B_1 and E fields of the Nova 8Tx/32Rx head coil. This was accomplished by designing microstripline coils, as this design allows for superior control over the B_1 field distribution. To achieve the target B and E fields, four parallel microstriplines per channel were utilized, with careful control of the currents flowing through each of these lines. The positioning of current sources within each channel was arbitrary, but pairs of assigned current sources were configured to ensure uniform current flow along the designated paths. The inner and outer diameters, as well as the lengths of the microstriplines, were determined based on the dimensions of the head coil. This methodology ensures that the coil's performance and field distribution characteristics closely match those of the reference phantom within the head coil, thereby facilitating comparable results in MRI applications.

Given the design comprises eight strips for four microstriplines, controlling the current flowing through these lines necessitates the injection of current sources in a paired configuration to create a loop route. To effectively manage the current in the eight strip, seven current sources were assigned to various parts of the design. This configuration was meticulously planned to achieve the desired magnetic fields, ensuring the performance and field distribution characteristics align with the target specifications. It is necessary to determine the B-fields corresponding to arbitrary current source values for a reference phantom. The superposition of these fields should be designed to closely approximate or match the desired fields, as follows:

$$B_{1,\text{desiredN}}(r) = \sum_{j}^{Ns} \alpha_j B_{1,\text{simN},j}(r) \tag{3.1}$$

Given that $B_{1,\text{desiredN}}$ represents the normalized channel-wise desired B fields for channel N in the unit of T, and $B_{1,\text{simN},j}$ represents the normalized fields produced by the jth source in channel N with the unit of T, while unitless α_j denotes the coefficient of the jth current source. The linear combination of these fields can be expressed in matrix form

$$\mathbf{B}_{1,\text{desiredN}} = \mathbf{B}_{1,\text{simN}}\boldsymbol{\alpha} \tag{3.2}$$

which

$$\mathbf{B}_{1,\text{desiredN}} = \begin{bmatrix} B_{1,\text{desiredN}}(r_1) \\ B_{1,\text{desiredN}}(r_2) \\ \vdots \\ B_{1,\text{desiredN}}(r_{Nv}) \end{bmatrix}, \boldsymbol{\alpha} = \begin{bmatrix} \alpha_1 \\ \alpha_2 \\ \vdots \\ \alpha_{Ns} \end{bmatrix}.$$

$$\mathbf{B}_{1,\text{simN}} = \begin{bmatrix} B_{1,\text{simN},1}(r_1) & B_{1,\text{simN},2}(r_1) & \cdots & B_{1,\text{simN},Ns}(r_1) \\ B_{1,\text{simN},1}(r_2) & B_{1,\text{simN},2}(r_2) & \cdots & B_{1,\text{simN},Ns}(r_2) \\ \vdots & \vdots & \ddots & \vdots \\ B_{1,\text{simN},1}(r_{Nv}) & B_{1,\text{simN},2}(r_{Nv}) & \cdots & B_{1,\text{simN},Ns}(r_{Nv}) \end{bmatrix},$$

Ns and Nv are the total number of current sources and voxel numbers inside a phantom respectively. Then the matrix form of the equation is:

$$\begin{bmatrix} B_{1,\text{desiredN}}(r_1) \\ B_{1,\text{desiredN}}(r_2) \\ \vdots \\ B_{1,\text{desiredN}}(r_{Nv}) \end{bmatrix} = \begin{bmatrix} B_{1,\text{simN},1}(r_1) & B_{1,\text{simN},2}(r_1) & \cdots & B_{1,\text{simN},Ns}(r_1) \\ B_{1,\text{simN},1}(r_2) & B_{1,\text{simN},2}(r_2) & \cdots & B_{1,\text{simN},Ns}(r_2) \\ \vdots & \vdots & \ddots & \vdots \\ B_{1,\text{simN},1}(r_{Nv}) & B_{1,\text{simN},2}(r_{Nv}) & \cdots & B_{1,\text{simN},Ns}(r_{Nv}) \end{bmatrix} \begin{bmatrix} \alpha_1 \\ \alpha_2 \\ \vdots \\ \alpha_m \end{bmatrix}.$$

The coefficients α_j are calculated through least-squares optimization to closely match the desired fields at a voxel location r inside the phantom. To calculate the $\boldsymbol{\alpha}$ vector we need the inversion of the $\mathbf{B}_{1,\mathrm{simN}}$. Since the $\mathbf{B}_{1,\mathrm{simN}}$ is in the size of Ns×Nv and not square, itis not invertible. to calculate these weights the optimization problem is then defined as:

$$\min_{\alpha} \|\mathbf{B}_{1,\mathrm{desiredN}} - \mathbf{B}_{1,\mathrm{simN}}\boldsymbol{\alpha}\|^2 \tag{3.3}$$

In this optimization problem, we are trying to determine the optimal coefficients $\boldsymbol{\alpha}$ such that the superposition of the simulated B_1 fields, weighted by these coefficients, matches the desired B_1 field as closely as possible. The objective is to minimize the difference (in a least-squares sense) between the desired B_1 field and the weighted sum of the simulated B_1 fields.

To find the optimal coefficients $\boldsymbol{\alpha}$, we use the Moore-Penrose pseudoinverse of $\mathbf{B}_{1,\mathrm{simN}}$. The solution is given by:

$$\boldsymbol{\alpha} = \mathbf{B}^{+}_{1,\mathrm{simN}}\mathbf{B}_{1,\mathrm{desiredN}} \tag{3.4}$$

Given that the columns of $\mathbf{B}_{1,\mathrm{simN}}$ are linearly independent because of assigning independent ideal currents, the solution for the optimal coefficients $\boldsymbol{\alpha}$ can be found using the Moore-Penrose pseudoinverse of $\mathbf{B}_{1,\mathrm{simN}}$, $\mathbf{B}^{+}_{1,\mathrm{simN}}$. The solution is given by:

$$\boldsymbol{\alpha} = \left(\mathbf{B}^{H}_{1,\mathrm{simN}}\mathbf{B}_{1,\mathrm{simN}}\right)^{-1}\mathbf{B}^{H}_{1,\mathrm{simN}}\mathbf{B}_{1,\mathrm{desiredN}} \tag{3.5}$$

where $\mathbf{B}^{H}_{1,\mathrm{simN}}$ denotes the conjugate transpose of $\mathbf{B}_{1,\mathrm{simN}}$.Incorporating both normalized electric fields ($\mathbf{E}$) and normalized magnetic fields ($\mathbf{B}$) in the calculations allows for a more comprehensive analysis of the field interactions. Consequently, the desired fields vector should include both $\mathbf{B}$ and $\mathbf{E}$ fields. The combined equation can be expressed as:

$$\mathbf{M}_{B1E,\text{desiredN}} = \mathbf{M}_{B1E,\text{simN}}\boldsymbol{\alpha} \tag{3.6}$$

$$\mathbf{M}_{B1E,\text{desiredN}} = \begin{bmatrix} \mathbf{M}_{B1E,\text{desiredN}} \\ \mathbf{M}_{B1E,\text{desiredN}} \end{bmatrix}$$

$$\mathbf{M}_{B1E,\text{simN}} = \begin{bmatrix} \mathbf{B}_{1,\text{simN},1} & \mathbf{B}_{1,\text{simN},2} & \cdots & \mathbf{B}_{1,\text{simN},m} \\ \mathbf{E}_{1,\text{simN},1} & \mathbf{E}_{1,\text{simN},2} & \cdots & \mathbf{E}_{1,\text{simN},m} \end{bmatrix}$$

The current coefficients for this case can be calculated as following:

$$\boldsymbol{\alpha} = \left(\mathbf{M}^{H}_{B1E,\text{simN}}\mathbf{M}_{B1E,\text{simN}}\right)^{-1}\mathbf{M}^{H}_{B1E,\text{simN}}\mathbf{M}_{B1E,\text{desiredN}} \tag{3.7}$$

3.2.1 Adjustment calibration of the System

Since we use ideal current sources instead of capacitors to tune and achieve the desired B_1 fields, changing the phantom will not affect the B_1 and E fields. This is because ideal current sources maintain a constant current regardless of the load impedance or changes in the surrounding environment. As a result, variations in the phantom's dielectric properties, such as conductivity or permittivity, do not influence the electromagnetic fields generated by the coil. In contrast, practical systems using real current sources would require adjustments due to the varying impedance introduced by different phantoms.

Optimizing a pTx system for different phantoms is crucial for ensuring accurate field generation. The optimization process is same with the process of predicting the coil which involves measuring the B_1 field produced by each coil element and adjusting the phase and amplitude settings to achieve the desired uniformity. This typically involves adjusting the complex values of the current sources based on experimental B_{1+} mappings:

$$\boldsymbol{\beta} = \left(\mathbf{B}'^{H}_{1+,\mathrm{sim}}\mathbf{B}'_{1+,\mathrm{sim}}\right)^{-1}\mathbf{B}'^{H}_{1+,\mathrm{sim}}\mathbf{B}_{1+,\mathrm{experiment}} \tag{3.8}$$

Where $\mathbf{B}'_{1+,\mathrm{sim}}$ is the B field produced by α current coefficients.

3.3 Verification of Electric Fields

In the context of MRI, verifying the electric fields generated by RF coils is essential for ensuring the safety and efficacy of imaging procedures. The relationship between the electric fields and the induced temperature rise in tissue-equivalent phantoms provides a reliable method for such verification. When RF fields are applied in MRI systems, they induce currents within conductive materials, leading to resistive heating. The resulting temperature increase can be measured and used to quantify the electric fields. This relationship forms the basis for verifying electric fields using temperature measurements. The Specific Absorption Rate (SAR), which quantifies the rate of RF energy absorption in tissues, serves as the key parameter in this process.

Phantoms made from tissue-equivalent materials, such as gels with known dielectric properties, are utilized to mimic human tissue accurately [32]. These phantoms provide a controlled environment for measuring temperature changes induced by RF fields. Fiber optic thermometers are strategically placed at various locations within the phantom to measure temperature changes [20]. Fiber optic sensors are preferred due to their immunity to electromagnetic interference.

RF pulses are applied to the MRI coil at the desired frequency and power level. The power levels and duration are carefully controlled to ensure safety and avoid excessive heating. Temperature is measured at different points within the phantom before, during, and after the application of RF pulses. Baseline temperatures are recorded, and temperature changes are monitored over time to ensure a thermally stable environment free from external influences.

The SAR is calculated using the measured temperature data. The formula used is:

$$\text{SAR} = \frac{c_p \cdot \Delta T}{\Delta t} \tag{3.9}$$

where c_p is the specific heat capacity of the phantom material, ΔT is the temperature rise, and Δt is the duration of the RF pulse [5]. The electric field strength is estimated from the SAR values using:

$$\text{SAR} = \sigma \cdot \frac{|E|^2}{\rho} \tag{3.10}$$

Rearranging this equation gives:

$$|E| = \sqrt{\frac{\text{SAR} \cdot \rho}{\sigma}} \tag{3.11}$$

where σ is the electrical conductivity of the phantom, E is the electric field strength, and ρ is the density of the phantom [3]. The calculated electric field values are compared with theoretical or simulated values. Any discrepancies indicate potential issues with the experimental setup, calibration errors, or differences in phantom properties [25]. Repeated measurements ensure consistency and reliability. Proper placement of temperature sensors and consistency in phantom properties are crucial for accurate verification. Experimental results are validated with electromagnetic simulations using software like HFSS or CST. Comparing simulated temperature rises with experimental data helps ensure accuracy and reliability of the verification process [6, 4]. By following this methodology, the electric fields generated by MRI RF coils can be accurately verified, ensuring both the safety and efficacy of MRI procedures.

Chapter 4

Materials and Methods

4.1 Magnetom 7T Whole-Body Scanner

The Magnetom Whole-Body Scanner (Siemens Healthcare, Erlangen, Germany) has a static field strength of 7T [33]. The MR signal is read out via up to 32 individual receive channels. The transmission of the RF pulses is done either in single-channel or multi-channel mode (pTx) with up to 8 channels. The RF amplifier delivers a total output power of up to 8 kW, with the output power being evenly distributed among the transmit channels in pTx mode [34].

In the 7T Siemens scanners, the maximum local SAR location changes with the phases and amplitudes of the RF signals applied to each of the pTx channels. The scanners consider this change in the local SAR calculation and use the VOP (virtual observation points) approach for fast safety calculations[35]. In this approach, the scanners calculate local SAR values at a limited set of points rather than the whole volume. This reduces the SAR calculation time significantly. The VOP approach has been proven to be accurate and fast in estimating maximum local SAR. However, since local SAR rather than local temperature rise is calculated, a safety margin in the power limit is necessary. Here, it is known that Siemens' RF safety limits are very conservative when applying RF pulses using their pTx system. While this is good for patient safety, it may prohibit RF-intense pulse sequence usage and significantly increase the total scan time.

4.2 Nova 8Tx/32Rx Coil

The MR coil used for the subsequent measurements, manufactured by Nova Medical, Inc. (Wilmington MA USA), is a multi-channel head coil (pTx coil), consisting of a transmit and a receive part [36].

The receive part of the coil consists of a 32-channel surface coil array [36]. The transmit part of the pTx coil, constructed as a volume coil, consists of eight independent transmit channels, each coupled to its own RF generator [36]. The transmit channels can also be combined to function as a single-channel transmit coil [36].

The advantage of this combination of volume and surface coils is improved SNR with simultaneously as homogeneous excitation as possible. Surface coils alone typically provide better SNR than volume coils because they receive the signal from only a small area. However, they produce a very inhomogeneous field distribution when used for excitation for the same reason. Therefore, surface coils combined in a coil array are preferably used for receiving the MR signal, while the excitation is performed with a volume coil with a larger outer diameter [37].

The pTx coil has a resonance frequency of 297.18 MHz. The transmit coils generate a circularly polarized RF field and have a maximum transmit power of 8 kW [36].

4.3 Nova pTx simulation data

The manufacturer of the Nova 8Tx/32Rx Coil provided the Nova pTx simulation data which involves preliminary results from broadband tuned simulations using

Remcom field software. In this simulation coil-coil coupling and copper losses is considered and normalized to 1W transmitted power. The data includes complex E field, B field, J field 3D matrices for both a Hugo human model and a spherical phantom, along with conductivity and density information for each axis within a Yee cell.

Simulations were performed with all coil elements present and reflected power was low. Field values need conversion into B_1 fields based on scanner pole orientation. Voxel sizes are 2x2x2mm, covering a 28x28x28cm area, with fields masked to regions containing tissue or the phantom. This data is proprietary and requires validation for SAR estimation and scanner use. The validation of the B_1 fields of the simulations is reported by Brenner et al. [38].

4.4 GUFI Phantom

The German Ultrahigh Field Imaging network (GUFI) is a collaborative effort comprising 13 sites across Germany and neighboring regions, all operating ultra-high field (UHF) MRI systems of 7T or 9.4T. The GUFI phantom was designed to closely mimic the dielectric properties of human tissues, utilizing a mixture of polyvinylpyrrolidone (PVP), salt, water, and agar to emulate brain and muscle tissues. This phantom, combined with a robust measurement protocol, enables consistent and comparable assessment of system performance across different sites. The head compartment, made from PMMA, is filled with a gel mixture that includes water, PVP, agar, and salt, designed to replicate brain tissue properties. These phantoms were distributed to four initial UHF sites for testing, each equipped with a 7T whole-body MRI system from Siemens Healthcare. The QA protocol includes measurements for RF coil performance, gradient and system stability, and verification of the phantom filling material's stability over time. Parameters such as B_1 mapping, noise correlation, and relaxometry were analyzed to ensure long-term consistency and reliability [39]. The conductivity of the phantom is 0.54 [S/m] and the permittivity of it is 52 with the mass density of 1050 [kg/m^3]. The dimensions of GUFI phantom is showed in Figure 4.1

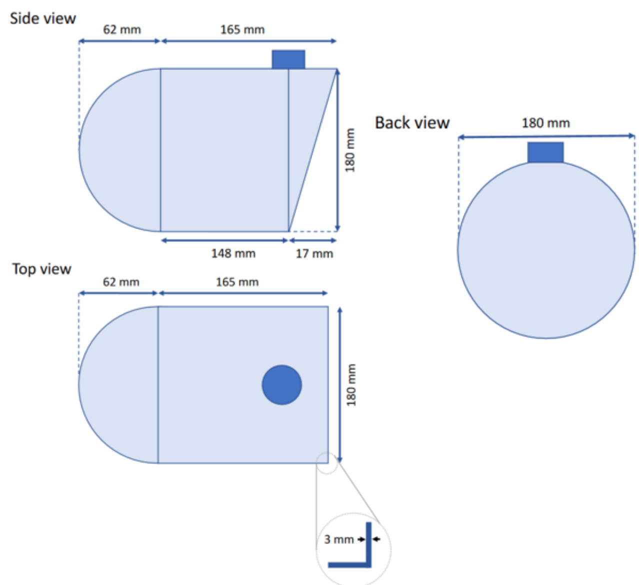

Figure 4.1: GUFI phantom dimensions

4.5 Electromagnetic (EM) Simulations

In this study, the High Frequency Structure Simulator (HFSS) by ANSYS was utilized to perform the electromagnetic simulations necessary for the design of 8Tx Nova coil. HFSS is a powerful tool in computational electromagnetics that provides accurate solutions for RF and microwave structures through its advanced finite element method (FEM) capabilities. The HFSS simulations were configured to accurately model the electromagnetic fields within the MRI environment at the operation frequency of 297.18 MHz equal to larmor frequency of H at 7T static field.

4.5.1 Simulation of the NOVA pTx Coils with Reference Phantom

In this section, we simulated eight parallel channels with four copper micro-strip-lines. No substrate has been utilized in the design. Each channel was assigned seven pairs of current sources to control the flowing currents in eight strips, as illustrated in Figure 4.2.

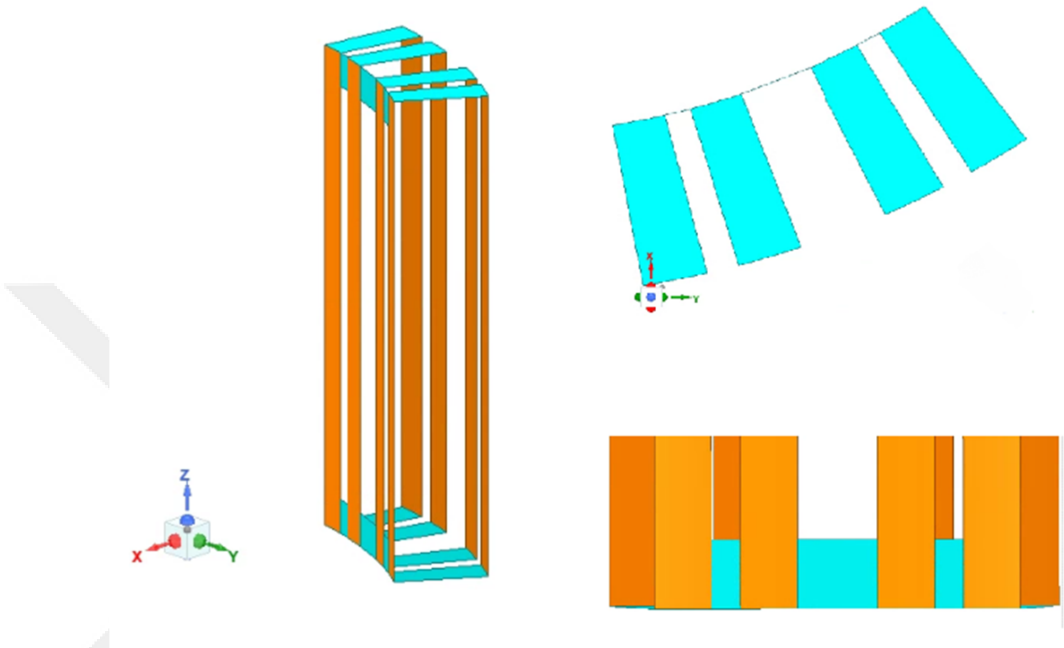

Figure 4.2: Configuration of the NOVA pTx coil simulation setup.Orange strips are configuring the RF coil with the material of copper, and the blue squars are the planes for injecting the current sources.

The reference spherical phantom provided by the coil manufacturer was positioned at the center of the coil setup (Figure 4.2). Due to the lack of detailed documentation on the exact placement and permittivity, two positions along the Y-axis and 50 and 70 permittivity were tested to determine the optimal placement and permittivity. The simulations were conducted to verify the RF magnetic field and the incident electric field within the radiation boundary, ensuring they matched the B_1 fields specified by the manufacturer. These results were subsequently utilized in MATLAB to predict the required current source values using Eq. 3.7.

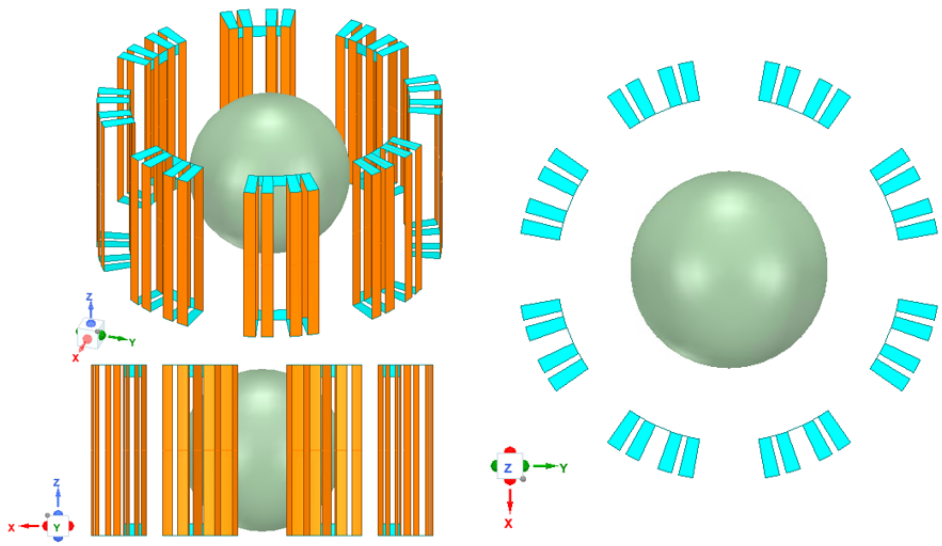

Figure 4.3: The reference spherical phantom used in the simulations.

4.5.2 Simulation of the NOVA pTx Coils with GUFI Phantom

After calculating the coefficients for arbitrary current values and optimizing the coil, the GUFI phantom, designed based on dimensions shown in Figure 4.1, was placed inside the coil design. The exact position of the phantom within the coil was predicted based on dimensional measurements. The primary B_{1+} fields of this design were used for further adjustment and calibration in MATLAB using Eq. 3.8.

4.6 GUFI Phantom B_{1+} Mapping

To verify the B_{1+} fields of the predicted coil, it was necessary to ensure consistency with other phantoms. The GUFI phantom was utilized for B_{1+} mapping. Measurements were conducted using the 8Tx/32Rx Nova head coil on a Magnetom 7T Whole-Body Scanner. The 3D-DREAM based B_1 mapping scheme was employed for B_{1+} mapping acquisition [38]. The B_{1+} magnitude and phase

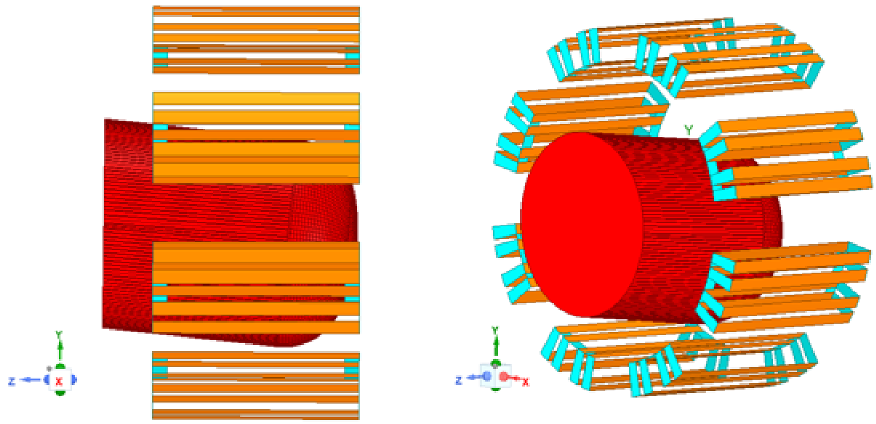

Figure 4.4: Configuration of the NOVA pTx coil with GUFI phantom.

field maps for Channel-wise mode, Circularly Polarized (CP) mode, Linear mode, and five Randomly Phased modes, along with the phantom mask and B_0, were provided by our collaborators from Bonn, Germany, and Trondheim, Belgium.

4.7 Heating Experiments

The temperature changes for Circularly Polarized (CP) mode, Linear mode, and five Randomly Phased modes were measured over a duration of 8 minutes by our collaborators in Trondheim. Three optical temperature probes were utilized to monitor the temperature variations induced by the RF heating pulse. These probes were strategically placed inside the phantom, approximately 120 degrees apart from each other, as illustrated in Figure 4.5. The precise placement of the probes was determined using a high-resolution scan, specifically the scaifield_mprage_UP_0.65iso.

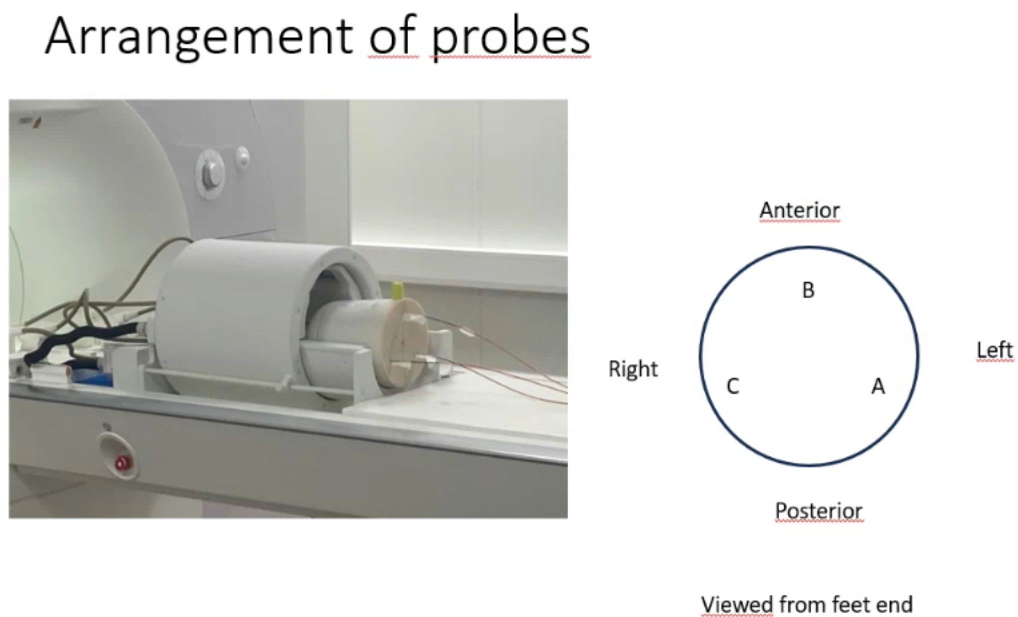

Figure 4.5: Configuration of the NOVA pTx coil heating experiment setup.

Chapter 5

Results

5.1 Nova coil prediction

The B_1 and E fields were simulated in Ansys HFSS (2022R1), with the complex vectors of B_1 and E fields exported for 10 mA current sources, denoted as $B_{1,\mathrm{simN},j}$ and $B_{1,\mathrm{simN},j}$, where N represents the channel labels and j represents the source labels. The current coefficients were computed using three distinct methods: first, employing Eq. 3.5 with the E fields; second, utilizing the same equation with the B_1 fields; and third, combining both E and B_1 fields in accordance with Eq. 3.7. These calculated complex current values were subsequently injected into the simulation setup to achieve the desired B_1 and E fields.

By controlling the symmetry of the B_{1+} field maps in the coronal or sagittal planes along the z-direction (Figure 5.1) and taking into account the design of the array coils, where each array consists of 8 parallel microstrip lines, we can ensure that the phantom is accurately positioned at the center of the coil along the z-axis. Furthermore, generally during the scan the phantom is centrally aligned along the x-axis.

Due to the unspecified permittivity and phantom placement in the y direction

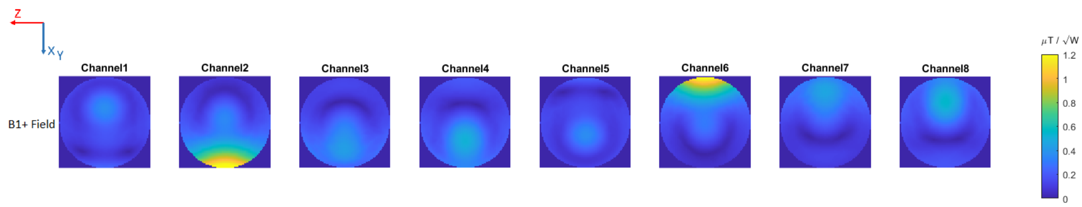

Figure 5.1: B_{1+} field maps in Coronal plane(Optimized using B_{1+} field.

in the provided documents, the α vector was calculated for two different placements in the y direction and for permittivity values of 50 and 70. Initially, for a spherical phantom with a conductivity of 1 S/m and a permittivity of 50, positioned at the center of the RF coil (phantom center at $y = 0$), a visual comparison between the our prediction and the Nova Simulation channel-wise B_1^+ maps on the phantom is presented in Figure 5.2. The corresponding scatter plots for E and B_1 are illustrated in Figure 5.3.

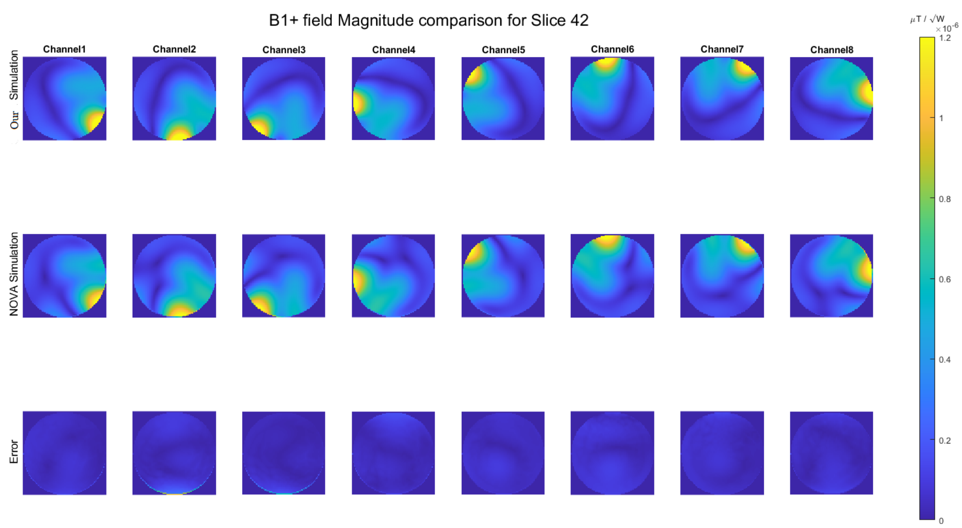

Figure 5.2: Comparison of axial view of simulated B_{1+} field magnitudes: our simulation (up) versus Nova simulation (down). The error is defined as the magnitude difference between the Nova and our simulations. A low error level indicates that the phase of the B_{1+} fields also matches closely, demonstrating the accuracy of the coil design.

The magnitude of the correlations between the respective B_1 maps was 0.96, revealing excellent agreement. The normalized root mean square error (NRMSE)

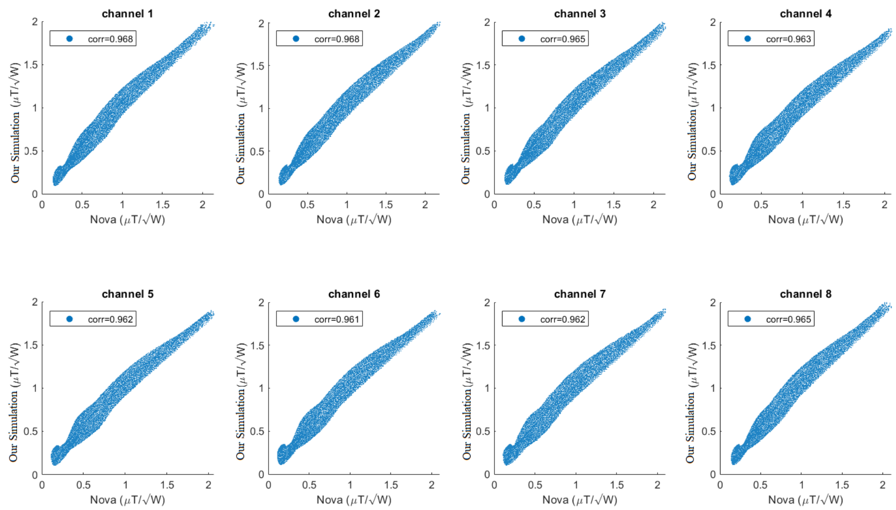

(a)

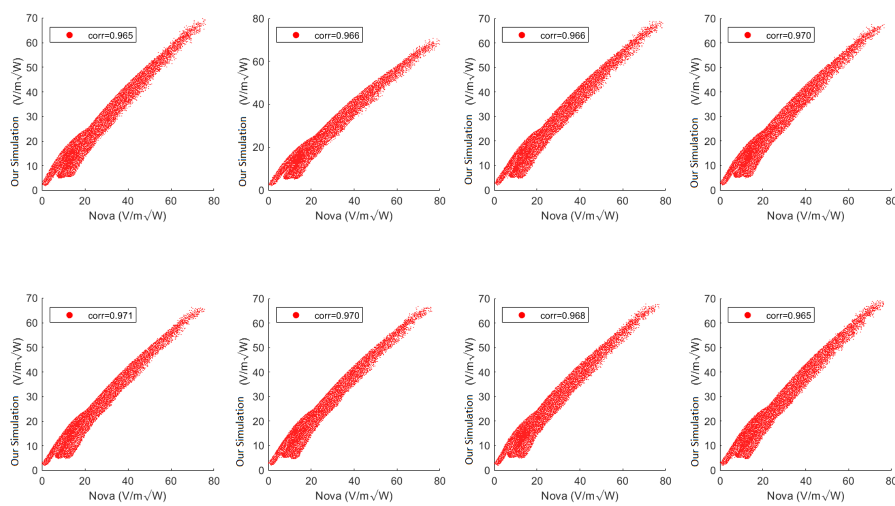

(b)

Figure 5.3: Scattered plots of the amplitudes of the B_1 and E field maps for permittivity of 50 shown in Figure 5.2. The magnitude of the correlation coefficient between the simulated and measured complex maps is provided for each channel.

between the maps is $7.8\% \pm 0.2$. The magnitude of the correlations between the respective E field maps was 0.97, revealing excellent agreement. The NMRSE between the maps is $6\% \pm 0.4$. The predictions for phantoms with permittivity values of 50 and 80 were conducted using two field datasets, and their results were compared through scatter plots of their corresponding electric (E) and magnetic (B_1) fields, as depicted in Figure 2.1. As shown in Figure 5.4, varying the permittivity and employing E and B_1 fields independently to obtain solutions do not result in significant differences in the outcomes. In all cases, there was excellent agreement between the predicted and observed values. This consistency suggests that the accuracy of the results at this step is not significantly influenced by the permittivity values or the type of field data (E or B_1 fields) used in the optimization process.

Therefore, the preferred approach moving forward is to utilize B_1 field data for solution determination, as B_1 fields are more readily measurable than E fields, making this method more practical for broader application in similar scenarios. We preferred to select optimization based on a permittivity of 80 since this value is close to the permittivity of the phantoms constructed for verifying the NOVA simulation data results.

In the following analysis, the B_{1+} fields produced by the predicted coil with a permittivity of 80 on the GUFI phantom will be compared between our simulations and experimental results.

After calculating the α solutions, we replaced the GUFI phantom with the reference spherical phantom and conducted simulations to evaluate the solution's performance with different phantoms. A visual comparison between the our prediction and the NOVA simulation B_{1+} maps on the GUFI phantom is presented in Figure 5.5.

As illustrated in Figure 5.5, in simulation results the level of B_{1+} field at the spot closer to the transmitter is brighter than experiments in channels 3, 4, 5, and 6, which correspond to the channels on the bottom side or in the -y direction. Conversely, in simulation results the level of B_{1+} field at the spot closer to the

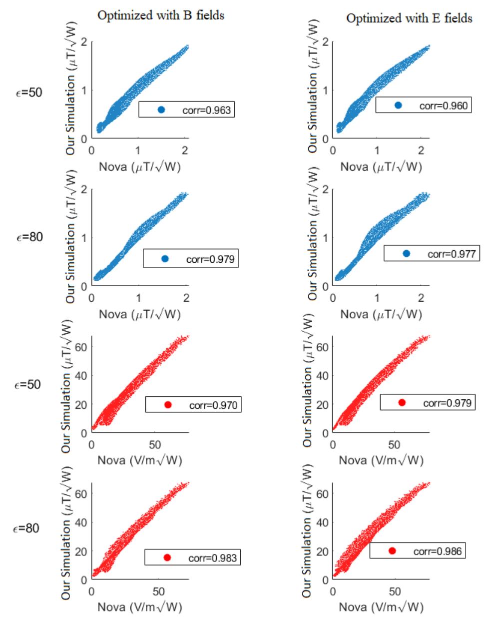

Figure 5.4: Scattered plots of the amplitudes of the E and B_1 field maps conducted using E and B_1 field data for reference phantom with permittivities of 50 and 80. The magnitude of the correlation coefficient between the simulated and measured complex maps is provided in each inset.

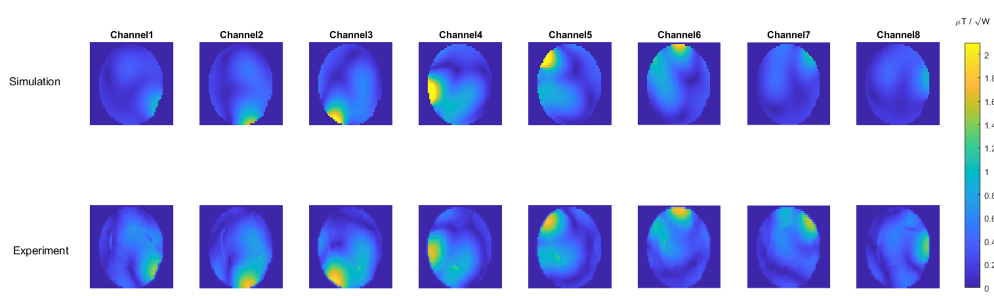

Figure 5.5: visual comparison of channelwise B_{1+} fields of our simulation and Experiments for optimization using reference with 80 epsilon and centered placement.

transmitter is darker than experiments in channels 1, 2, 7, and 8, which are located on the top side or in the +y direction. This indicates that the placement of the phantom along the y-axis is incorrect. Given our confidence in the placement of the GUFI phantom, we must adjust the position of the spherical phantom and calculate new solutions for adjusted placement of reference phantom. Specifically, the reference phantom should be moved closer to the bottom channels or displaced in the -y direction. Based on the dimensional measurements and placement of GUFI phantom, a maximum displacement of 25 mm in the -y direction was selected.The resulting B_{1+} fields for the GUFI phantom after adjustments in the y-direction with displacements of -25 mm, -15 mm, and 0 mm are shown in Figure 5.6 .

The correlation coefficients between the magnitudes of the channel-wise B_{1+} fields for solutions at displacements of $y = 0\,\mathrm{mm}$, $y = -15\,\mathrm{mm}$, and $y = -25\,\mathrm{mm}$ are 0.83 ± 0.08, 0.86 ± 0.06, and 0.88 ± 0.05, respectively. Additionally, the normalized root mean square error (NRMSE) between the magnitudes of the channel-wise B_{1+} fields for these displacements are $10.7\% \pm 3.68$ for $y = 0\,\mathrm{mm}$, $9.05\% \pm 3.30$ for $y = -15\,\mathrm{mm}$, and $9.14\% \pm 5.58$ for $y = -25\,\mathrm{mm}$.

These results suggest that the configuration with a $y = -15\,\mathrm{mm}$ displacement provides a slightly better correlation and lower NRMSE compared to the other configurations, indicating improved agreement between the simulated and reference fields. This is particularly important for optimizing the performance of the coil in applications where precise B_{1+} field distribution is critical. The higher correlation and lower NRMSE values indicate that the electromagnetic behavior of the coil is more accurately captured at this displacement, leading to better field homogeneity.

To further evaluate the phase matching of the designed coil, random-phase RF shimming was applied, and the resulting magnitudes from simulations were compared with experimental measurements. The visual comparison of these randomly phased RF shims is presented in Figure 5.7.

The correlations between the magnitudes of the random phased B_{1+} fields for

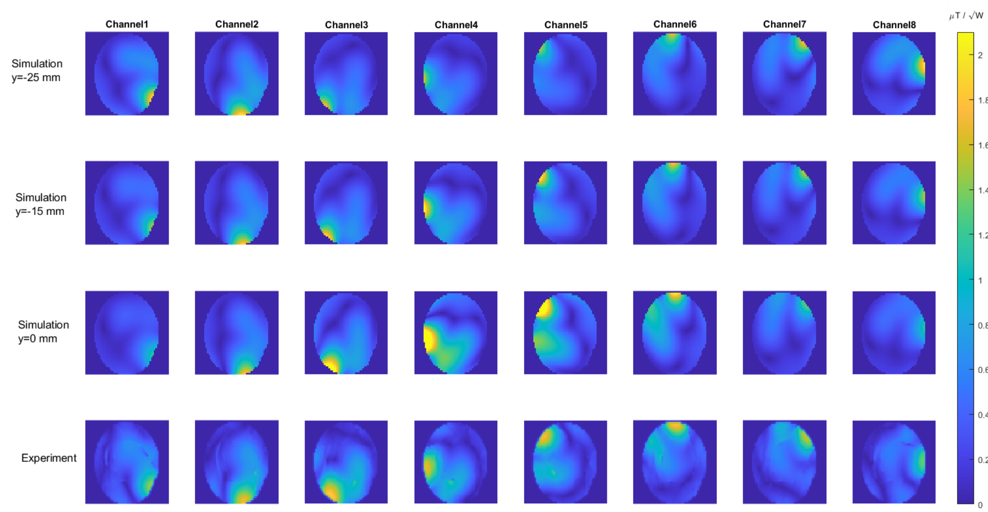

(a)

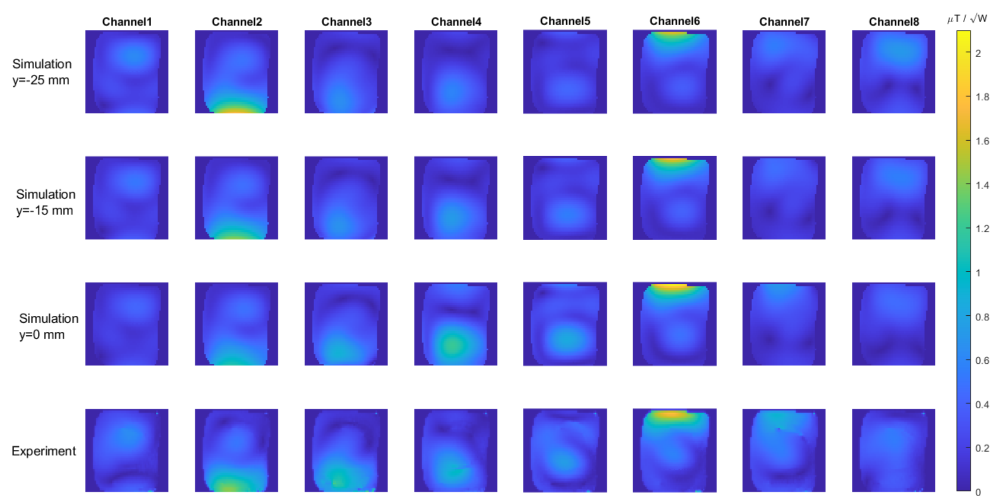

(b)

Figure 5.6: visual comparison of channelwise B_{1+} fields of our simulation with the displacements of -25, -15, 0 mm in Y direction and Experiment for optimization using 80 epsilon in (a) axial and (b) coronal plane.

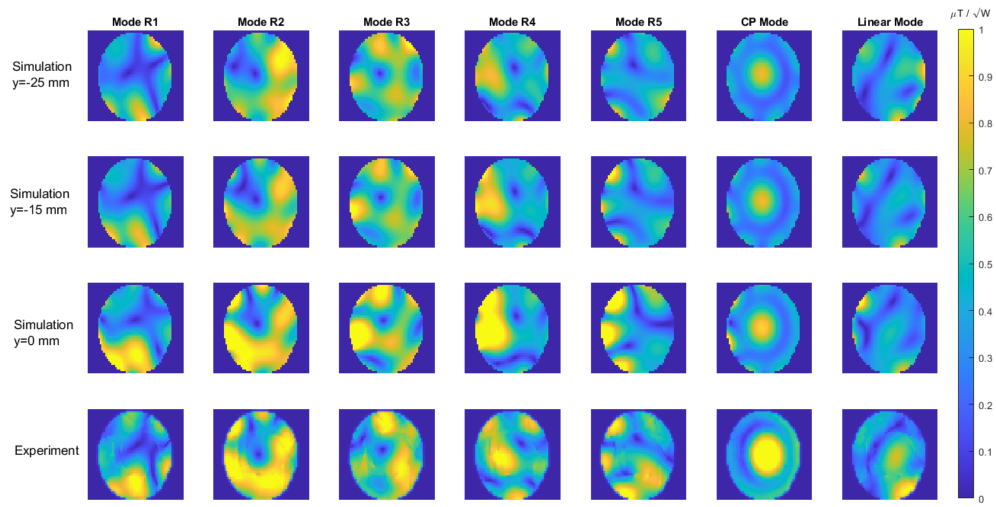

(a)

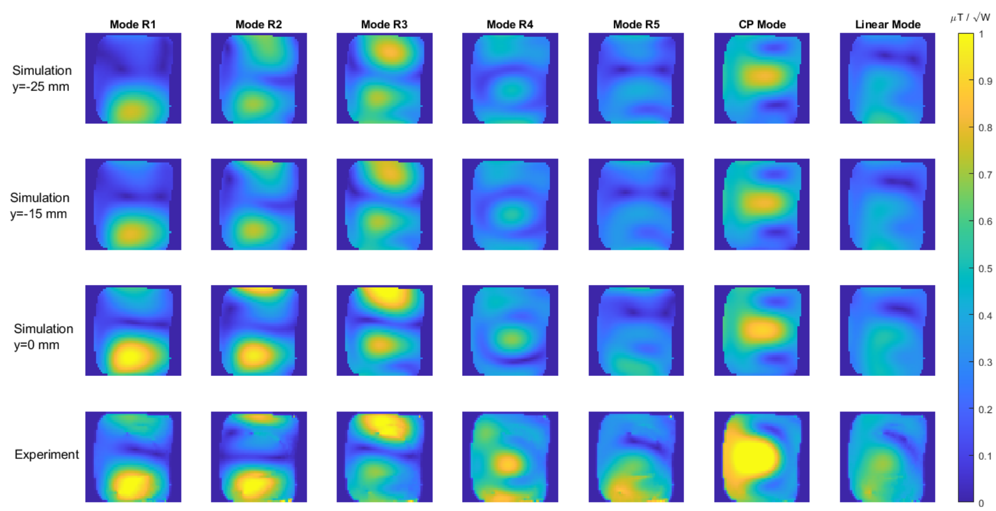

(b)

Figure 5.7: visual comparison of B_{1+} fields of our simulation with the displacements of -25, -15, 0 mm in Y direction for random-phase shimming and Experiment for optimization using 80 epsilon in (a) axial and (b) coronal plane.

solutions at displacements of $y = 0\,\text{mm}$, $y = -15\,\text{mm}$, and $y = -25\,\text{mm}$ are 0.62 ± 0.11, 0.69 ± 0.10, and 0.67 ± 0.22, respectively. The corresponding NRMSE values are $78.49\% \pm 20.3$ for $y = 0\,\text{mm}$, $72.16\% \pm 26.76$ for $y = -15\,\text{mm}$, and $47.89\% \pm 15.16$ for $y = -25\,\text{mm}$.

The significantly higher NRMSE values and lower correlations observed in the random-phase shimming analysis indicate a larger discrepancy between the simulated and experimental data in this context. This suggests that the phase alignment is more challenging to achieve across the different displacements, which could be attributed to the complex interaction of the RF fields within the coil setup. Notably, the configuration with $y = -15\,\text{mm}$ continues to show relatively better performance, with both lower NRMSE and higher correlation, reinforcing its suitability for achieving more uniform B_{1+} fields. Overall, the results demonstrate that careful adjustment of the displacement, particularly at $y = -15\,\text{mm}$, is key to optimizing both the magnitude and phase alignment of the B_{1+} fields. The findings also highlight the importance of considering both magnitude and phase when evaluating coil performance for high-field MRI applications. Since we are using ideal current sources, further improvements are needed in adjusting the current sources. When changing the phantom, it will affect the current source tuning and load. This is because the electrical loading of the coil is influenced by the dielectric properties of the phantom, which directly impacts the coil's resonance and the distribution of the generated electromagnetic fields. Without proper adjustments, the system might not maintain optimal tuning, leading to degraded performance in both the magnitude and phase of the B_{1+} fields.

By employing the Least Mean Square (LMS) approach, we sought to determine solutions that achieve a close match with the B_{1+} field distributions observed in the experimental data. The comparison of the channel-wise optimized B_{1+} fields is illustrated in Figure 5.8. For the optimization solutions using the GUFI phantom, the correlation between the magnitudes of the channel-wise B_{1+} fields is 0.83 ± 0.05, with a corresponding NRMSE value of $25.64\% \pm 4.23$. These results indicate a strong agreement between the optimized and experimental B_{1+} field distributions, reflecting the effectiveness of the LMS method in achieving the desired field characteristics.

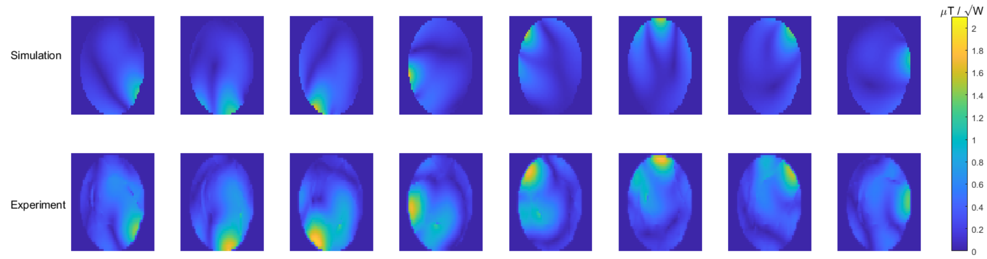

(a)

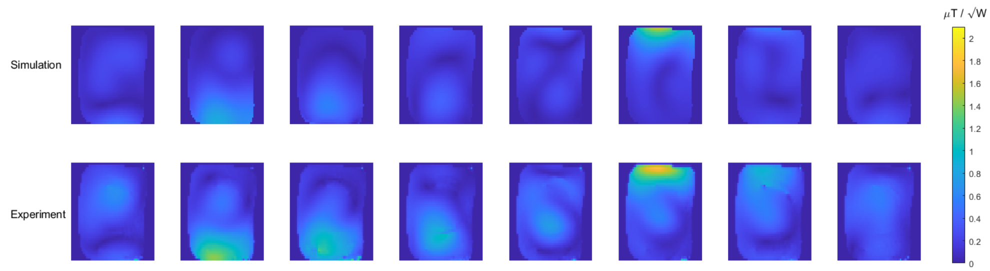

(b)

Figure 5.8: visual comparison of channelwise B_{1+} fields of our simulation optimized using GUFI Experiment results in (a) axial and (b) coronal plane.

Furthermore, a comparison of the B_{1+} fields for the randomly phased setting is done. In this scenario, the correlation between the magnitudes of the channel-wise B_{1+} fields for the optimization solutions using the GUFI phantom is 0.80 ± 0.09, while the corresponding NRMSE is observed to exceed 50%. This higher error suggests that the random-phase configuration poses greater challenges in accurately replicating the experimental B_{1+} fields, highlighting the need for further refinement in optimizing such complex field scenarios.

Chapter 6

Discussion, Conclusion and Future work

The primary aim of this study was to develop and implement temperature-based RF safety assessment techniques for cerebellar imaging using 7T MRI systems, specifically focusing on Spinocerebellar Ataxias (SCAs). This involved predicting the electromagnetic behavior of the Nova coil to ensure accurate and safe imaging, as the electromagnetic simulation design was not provided by the manufacturer. Accurate prediction of the coil's behavior is crucial, as it directly impacts the safety and quality of MRI scans, particularly in managing RF exposure and minimizing tissue heating. Considering this, our study aimed to address the question: How can we accurately predict the electromagnetic behavior of the Nova coil to enhance RF safety and imaging quality in 7T MRI systems?

Through the simulation and modeling of the Nova 8Tx coil, we aimed to replicate the electromagnetic behavior observed in experiments. While the simulations provided valuable insights, some discrepancies were noted between the predicted and experimental electromagnetic fields. These differences highlight the complexities inherent in predicting the coil's behavior when the original manufacturer's electromagnetic simulation data is not available. The results suggest that while the predicted coil design captured key aspects of the B_{1+} field distribution, there is room for improvement in aligning the simulation with the actual performance observed in experimental measurements.

Focusing specifically on the reference displacement at $y = -15\,\text{mm}$, the correlation coefficient between the magnitudes of the channel-wise B_{1+} fields was 0.86 ± 0.06, and the normalized root mean square error (NRMSE) was $9.05\% \pm 3.30$. These results indicate a relatively strong alignment between the magnitudes of simulated and experimental B_{1+} field distributions. The high correlation and low NRMSE values suggest that this configuration captures the key characteristics of the fields magnitude with minimal error. The $y = -15\,\text{mm}$ displacement thus emerged as the optimal configuration among those tested, showing a favorable trade-off between accuracy and error metrics.

However, despite these positive results, challenges remain in capturing the finer phase results of the electromagnetic fields, especially when considering random-phase shimming configurations. In such cases, phase alignment becomes more difficult to achieve consistently, leading to greater deviations and higher NRMSE values.

The approach of using a reference phantom provided a reliable basis for Optimization and offered a stable reference point for comparing different scenarios. However, the deviations observed indicate that further refinement is needed, particularly in capturing the fine details that influence the electromagnetic fields in more complex phantom configurations.

One significant aspect of the study is the use of ideal current sources in our simulations. Since ideal current sources were implemented, changing the phantom did not affect the current source behavior. While this approach makes the simulation easier, it has limitations because it does not fully consider the effects of different loading conditions that occur with various phantoms in real situations. To address this limitation, one potential solution involves using the equivalent capacitance values of the calculated current source solutions, which requires knowing the exact placements of the capacitors in the fabricated coil. However, since these placements were unclear, we did not pursue this method.

Instead, a more practical approach would involve optimizing the system using experimental B_{1+} fields by minimum least squares methods, which allows for better adaptability in real-world applications.

Despite using these methods, the results continued to demonstrate significant errors. A key factor contributing to this discrepancy is likely the variation in the data used across the optimization stages. In the initial optimization with the reference phantom, we utilized simulation data comprising complex B_1 fields components in three directions, providing a more comprehensive and detailed dataset for accurately modeling the electromagnetic behavior.

In contrast, when optimizing with experimental results, the process relied solely on complex B_{1+} values, which provide less detailed information compared to the full set of B_1 components. This reduction in data likely contributed to the increased error observed in the results. The limited scope of the data used in the optimization likely led to under fitting, where the model fails to fully capture the complexity of the electromagnetic fields. Additionally, the presence of noise and other inaccuracies in the experimental measurements further compounded the errors. These factors, combined with the limitations of optimizing with fewer field components, made it more difficult to accurately model the coil's behavior, leading to greater deviations between the predicted and actual electromagnetic fields.

To further illustrate these discrepancies, a detailed comparison between the experimental and simulated electric field ($|E|$) values across different configurations is provided in Table 6.1. This table highlights the variations in the $|E|$ fields for different modes, demonstrating the underestimation of simulated values compared to experimental measurements, particularly in linear and random-phase settings.

Table 6.1 shows the comparison between the experimental and simulated electric field ($|E|$) values for the solution with a $y = -15\,\mathrm{mm}$ displacement across different configurations. The error in the calculated and experimental results need to be investigated. Unfortunately, this important step was not completed

	$\lvert E\rvert_{A,\text{exp}}$ (V/m)	$\lvert E\rvert_{B,\text{exp}}$ (V/m)	$\lvert E\rvert_{C,\text{exp}}$ (V/m)	$\lvert E\rvert_{A,\text{sim}}$ (V/m)	$\lvert E\rvert_{B,\text{sim}}$ (V/m)	$\lvert E\rvert_{C,\text{sim}}$ (V/m)
Linear Mode 1	16	70	43	12	22	21
CP Mode	38	48	38	23	23	27
Random Phase 1	61	37	28	14	30	25
Random Phase 2	46	57	40	29	39	29
Random Phase 3	56	38	71	45	40	44
Random Phase 4	26	16	38	23	37	34
Random Phase 5	31	59	57	30	20	27

Table 6.1: Comparison of Experimental and Simulation E Field Values

in this thesis and left as a future work.

Given these observations, it is advisable to optimize the current source values based primarily on B_{1+} field measurements for each different phantom. While direct optimization using $|E|$ fields is not feasible due to limited data, fine-tuning the current sources based on B_{1+} measurements can still lead to improvements in the $|E|$ field distribution indirectly. By tailoring the current source settings to the specific electromagnetic environment of each phantom, this approach can result in improved field uniformity and overall performance. Consequently, the system remains optimally tuned regardless of the phantom used, minimizing errors and enhancing the accuracy of both the B_{1+} field distribution and the $|E|$ fields.

In summary, this study highlights both the potential and challenges of predicting the electromagnetic behavior of MRI coils when limited manufacturer data is available. The findings demonstrate that, while initial simulations and optimizations can provide valuable insights into coil performance, real-world complexities such as incomplete data, idealized current source models, and experimental inaccuracies significantly impact prediction accuracy. Despite these challenges, the study underscores the importance of integrating empirical measurements with refined simulations to bridge the gap between theory and practice.

While this study has made strides in understanding and predicting coil behavior in the absence of detailed manufacturer data, several avenues for future research remain. One area involves investigating the unknowns in coil design when using reference phantoms. Designing and optimizing the coil with a reference phantom requires adjusting numerous unknown parameters, such as placement of reference phantom, dielectric properties of loading phantoms, and loading conditions, to ensure the coil performs as expected with different phantoms. Future work should systematically investigate and quantify these factors to enhance the reliability and accuracy of coil designs based on reference phantoms.

Additionally, enhancing experimental validation through more extensive measurement techniques is essential. Incorporating high-resolution temperature mapping across multiple points within the phantom or using electric field probes to measure the electric fields generated by the coil directly would provide more comprehensive data for validation. Comparing these detailed measurements with simulation results could reveal finer discrepancies and guide further refinements in both the simulation models and the coil design itself.

Another key focus is mitigating noise and experimental inaccuracies. Reducing the impact of noise and inaccuracies in measurements is crucial for obtaining more reliable data. This could be achieved by refining measurement techniques or applying advanced filtering methods to improve signal quality.

Moreover, adaptive and real-time optimization approaches could be explored. Leveraging machine learning and adaptive algorithms could enable real-time adjustments in coil configurations, leading to more robust and flexible models that dynamically adapt to various conditions and phantom scenarios.

Lastly, expanding the scope to clinical applications is vital. Future research should investigate how these techniques can be applied in broader clinical settings, particularly in optimizing RF safety and imaging quality for a range of neurological conditions beyond SCAs.

By addressing these areas, future work can build on the foundations laid by this study, moving closer to achieving highly accurate and reliable predictions of electromagnetic behavior in high-field MRI systems. Such advancements will be pivotal in enhancing the safety, quality, and adaptability of MRI technology in both research and clinical applications.

Bibliography

[1] A. Beqiri, *Parallel transmission mri for optimised cardiac imaging and improved safety.* PhD thesis, King's College London, 2015.

[2] International Electrotechnical Commission, *Medical Electrical Equipment. Part 2-33: Particular Requirements for the Safety of Magnetic Resonance Equipment for Medical Diagnosis.* IEC 60601-2-33, Geneva, Switzerland: International Electrotechnical Commission, 2022.

[3] N. Boulant, X. Wu, G. Adriany, S. Schmitter, K. Uğurbil, and P.-F. Van de Moortele, "Direct control of the temperature rise in parallel transmission by means of temperature virtual observation points: simulations at 10.5 tesla," *Magnetic resonance in medicine*, vol. 75, no. 1, pp. 249–256, 2016.

[4] G. Eichfelder and M. Gebhardt, "Local specific absorption rate control for parallel transmission by virtual observation points," *Magnetic resonance in medicine*, vol. 66, no. 5, pp. 1468–1476, 2011.

[5] C. M. Collins, W. Liu, J. Wang, R. Gruetter, J. T. Vaughan, K. Ugurbil, and M. B. Smith, "Temperature and sar calculations for a human head within volume and surface coils at 64 and 300 mhz," *Journal of Magnetic Resonance Imaging: An Official Journal of the International Society for Magnetic Resonance in Medicine*, vol. 19, no. 5, pp. 650–656, 2004.

[6] J. Lee, M. Gebhardt, L. L. Wald, and E. Adalsteinsson, "Local sar in parallel transmission pulse design," *Magnetic Resonance in Medicine*, vol. 67, no. 6, pp. 1566–1578, 2012.

[7] S. Orzada, T. M. Fiedler, H. H. Quick, and M. E. Ladd, “Local sar compression algorithm with improved compression, speed, and flexibility,” *Magnetic resonance in medicine*, vol. 86, no. 1, pp. 561–568, 2021.

[8] S. Orzada, H. H. Quick, M. E. Ladd, A. Bahr, T. Bolz, P. Yazdanbakhsh, K. Solbach, and A. K. Bitz, “A flexible 8-channel transmit/receive body coil for 7 t human imaging,” in *Proc Intl Soc Mag Reson Med*, vol. 17, p. 2999, 2009.

[9] R. W. Brown, Y.-C. N. Cheng, E. M. Haacke, M. R. Thompson, and R. Venkatesan, *Magnetic resonance imaging: physical principles and sequence design*. John Wiley & Sons, 2014.

[10] D. I. Hoult and R. Richards, “The signal-to-noise ratio of the nuclear magnetic resonance experiment,” *Journal of Magnetic Resonance (1969)*, vol. 24, no. 1, pp. 71–85, 1976.

[11] E. Moser, F. Stahlberg, M. E. Ladd, and S. Trattnig, “7-t mr—from research to clinical applications?,” *NMR in Biomedicine*, vol. 25, no. 5, pp. 695–716, 2012.

[12] O. Kraff, A. Fischer, A. M. Nagel, C. Mönninghoff, and M. E. Ladd, “Mri at 7 tesla and above: demonstrated and potential capabilities,” *Journal of Magnetic Resonance Imaging*, vol. 41, no. 1, pp. 13–33, 2015.

[13] P. Harvey, “High field imaging-an overview of technical challenges,” in *Proceedings of the International Society for Magnetic Resonance in Medicine*, 2006.

[14] Z.-P. Liang and P. C. Lauterbur, *Principles of magnetic resonance imaging*. SPIE Optical Engineering Press Bellingham, 2000.

[15] D. G. Norris, “High field human imaging,” *Journal of Magnetic Resonance Imaging: An Official Journal of the International Society for Magnetic Resonance in Medicine*, vol. 18, no. 5, pp. 519–529, 2003.

[16] F. R. Korosec, “Mri imaging options,” 2006.

[17] U. Katscher and P. Börnert, "Parallel rf transmission in mri," *NMR in Biomedicine: An International Journal Devoted to the Development and Application of Magnetic Resonance In vivo*, vol. 19, no. 3, pp. 393–400, 2006.

[18] P. Ullmann, S. Junge, M. Wick, F. Seifert, W. Ruhm, and J. Hennig, "Experimental analysis of parallel excitation using dedicated coil setups and simultaneous rf transmission on multiple channels," *Magnetic Resonance in Medicine: An Official Journal of the International Society for Magnetic Resonance in Medicine*, vol. 54, no. 4, pp. 994–1001, 2005.

[19] Y. Zhu, "Parallel excitation with an array of transmit coils," *Magnetic Resonance in Medicine: An Official Journal of the International Society for Magnetic Resonance in Medicine*, vol. 51, no. 4, pp. 775–784, 2004.

[20] H. Homann, *SAR prediction and SAR management for parallel transmit MRI*, vol. 16. KIT Scientific Publishing, 2014.

[21] A. Hoyos-Idrobo, P. Weiss, A. Massire, A. Amadon, and N. Boulant, "On variant strategies to solve the magnitude least squares optimization problem in parallel transmission pulse design and under strict sar and power constraints," *IEEE transactions on medical imaging*, vol. 33, no. 3, pp. 739–748, 2013.

[22] P.-F. Van de Moortele, C. Akgun, G. Adriany, S. Moeller, J. Ritter, C. M. Collins, M. B. Smith, J. T. Vaughan, and K. Uğurbil, "B1 destructive interferences and spatial phase patterns at 7 t with a head transceiver array coil," *Magnetic resonance in medicine*, vol. 54, no. 6, pp. 1503–1518, 2005.

[23] J. C. McGowan, "Basic principles of magnetic resonance imaging," *Neuroimaging Clinics of North America*, vol. 18, no. 4, pp. 623–636, 2008.

[24] D. J. Larkman and R. G. Nunes, "Parallel magnetic resonance imaging," *Physics in Medicine & Biology*, vol. 52, no. 7, p. R15, 2007.

[25] I. Graesslin, P. Vernickel, P. Börnert, K. Nehrke, G. Mens, P. Harvey, and U. Katscher, "Comprehensive rf safety concept for parallel transmission mr," *Magnetic Resonance in Medicine*, vol. 74, no. 2, pp. 589–598, 2015.

[26] X. Zhang, K. Ugurbil, and W. Chen, "Microstrip rf surface coil design for extremely high-field mri and spectroscopy," *Magnetic Resonance in Medicine: An Official Journal of the International Society for Magnetic Resonance in Medicine*, vol. 46, no. 3, pp. 443–450, 2001.

[27] G. C. Wiggins, R. Brown, and K. Lakshmanan, "High-performance radiofrequency coils for 23na mri: brain and musculoskeletal applications," *NMR in Biomedicine*, vol. 29, no. 2, pp. 96–106, 2016.

[28] J. Vaughan, "High frequency coils for clinical nuclear magnetic resonance imaging and spectroscopy," *Phys Med*, vol. 9, pp. 147–153, 1994.

[29] C.-H. Choi, A. Webb, S. Orzada, M. Kelenjeridze, N. J. Shah, and J. Felder, "A review of parallel transmit arrays for ultra-high field mr imaging," *IEEE Reviews in Biomedical Engineering*, vol. 17, pp. 351–368, 2023.

[30] US Food and Drug Administration, "Criteria for significant risk investigations of magnetic resonance diagnostic devices-guidance for industry and food and drug administration staff," 2014. Available at: `https://www.fda.gov/regulatory-information/search-fda-guidance-documents/criteria-significant-risk-investigations-magnetic-resonance-diagnostic-device`

[31] A. Hoyos-Idrobo, P. Weiss, A. Massire, A. Amadon, and N. Boulant, "On variant strategies to solve the magnitude least squares optimization problem in parallel transmission pulse design and under strict sar and power constraints," *IEEE transactions on medical imaging*, vol. 33, no. 3, pp. 739–748, 2013.

[32] C. Gabriel and S. Gabriel, "Compilation of the dielectric properties of body tissues at rf and microwave frequencies," 1996.

[33] Siemens AG, *Magnetom 7T Product Brochure*, 2013. Siemens Healthcare, Erlangen, Germany.

[34] Siemens AG, *Magnetom 7T Operator Manual - Tx Array System syngo MR B17*, 2012. Siemens Healthcare, Erlangen, Germany.

[35] A. J. Fagan, A. K. Bitz, I. M. Björkman-Burtscher, C. M. Collins, V. Kimbrell, A. J. Raaijmakers, and I. S. Committee, "7t mr safety," *Journal of Magnetic Resonance Imaging*, vol. 53, no. 2, pp. 333–346, 2021.

[36] Nova Medical, Inc., *Operator Handbook 7T Head Transmit Coil with Thirty-Two Channel Array Model NM008B-32-7S*, 2013. Wilmington MA USA.

[37] E. Boskamp, "Improved surface coil imaging in mr: decoupling of the excitation and receiver coils.," *Radiology*, vol. 157, no. 2, pp. 449–452, 1985.

[38] D. Brenner, D. H. Tse, P. J. Ledden, C. Neumann, and T. Stöcker, "Rapid and accurate ptx b1 mapping using 3dream with dual interferometry," in *Proceedings of the international society for magnetic resonance in medicine scientific meeting and exhibition*, vol. 109, 2015.

[39] M. N. Voelker, O. Kraff, E. Pracht, A. Wollrab, A. K. Bitz, T. Stöcker, H. H. Quick, O. Speck, and M. E. Ladd, "Quality assurance phantoms and procedures for uhf mri–the german ultrahigh field imaging (gufi) approach," in *Proceedings of the Annual Meeting ISMRM. Honolulu*, vol. 3912, 2017.